# 3 PROGRAMMABLE APODIZERS AND FRESNEL LENSES

## 3.1 Image formation and non-uniform transmission pupils

In this Section we describe the mathematical formulation and the method we use to calculate the complex amplitude at a point in the image space for an optical system. The calculation method is based on the works of Hopkins and Yzuel [Hop70] and Yzuel and Arlegui [Yzu80]. The mathematical formulation is based on the scalar theory of diffraction and the calculation method is valid for optical systems with rotational symmetry.

We consider an extra-axial point in the object space, emitting monochromatic light. The situation in the image space is expressed in Figure 3.1: $\overline{E}'O'$ is the optical axis of the system and the exit pupil is in $\overline{E}'$. $O'\overline{Q}'Q'$ is the image plane. The paraxial image of the object point is formed at $\overline{Q}'$ and $\overline{E}'\overline{Q}'$ is the principal ray of the pencil emerging from the exit pupil. Rectangular

coordinates are used with origin at $\bar{E}'$ at the exit pupil plane. The coordinates $(X', Y')$ are perpendicular to the optical axis, with the $Y'$ axis lying in the meridian plane containing $\bar{Q}'$. $(x', h')$ are the rectangular coordinates of $Q'$ with respect to $\bar{Q}'$ in the image plane. For convenience only, diagrams will be shown in two dimensions, although the formulae will be treated using all three dimensions.

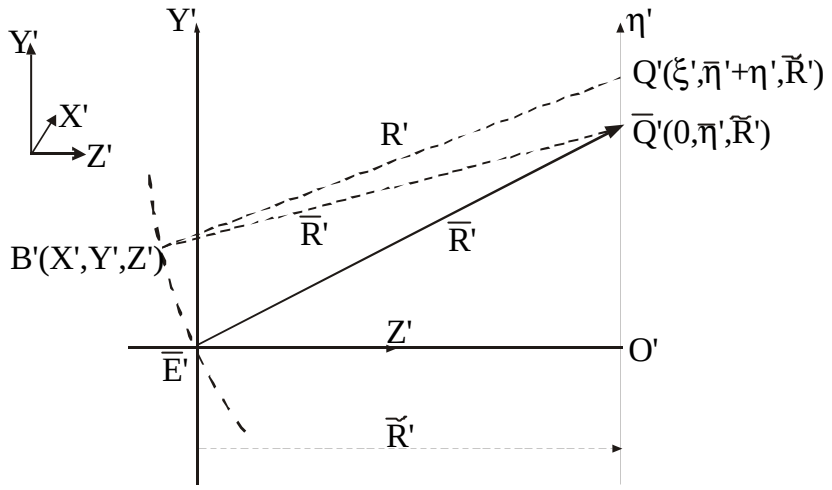


**Figure 3.1.** Diagram of the coordinates in the image space.

The wave aberration $W(X', Y')$ of the pencil forming the image at $\bar{Q}'$ is specified with respect to the reference sphere $\bar{E}'B'$, with centre at $\bar{Q}'$. We want to find the complex amplitude at any point $Q'$ in the image plane. This is given, within the Kirchhoff approximation, by the formula

$$U_{Q'} = \frac{i}{\lambda} \iint_{A'} f(X', Y') \frac{\exp(-ikR')}{R'} dA \qquad (3\text{-}1)$$

where $k = 2\pi/\lambda$, $\lambda$ being the wavelength. The function $f(X', Y')$ is called the pupil function and it expresses the complex amplitude over the reference sphere, as a function of the coordinates $(X', Y')$ of the point $B'$ on the reference sphere, so that

$$f(X', Y') = \begin{cases} \tau(X', Y') \exp[ikW(X', Y')] & \text{within } A' \\ 0 & \text{outside } A' \end{cases} \qquad (3\text{-}2)$$

where $t(X',Y')$ is the amplitude over the reference sphere. In the case the system has a uniform transmission, the function $t(X',Y')$ has a constant value over the region $A'$ of the pupil.

With the usual approximations [Hop70] the complex amplitude at $Q'$ is found to be

$$U_{Q'} = \frac{i\,exp[-ie(x',h')]}{l\bar{N}'\,\bar{R}'} exp[-ik\bar{R}']F(x',h') \tag{3-3}$$

where

$$e(x',h') = \frac{2p}{l}\left[\frac{x'^2+h'^2+2\bar{r}'\,h'}{2\bar{R}'}\right] \tag{3-4}$$

$$F(x',h') = \iint_{A'} f(X',Y') exp\left[i2p\,\frac{(x'\,X'+h'\,Y')}{l\bar{R}'}\right] dX'\,dY' \tag{3-5}$$

and $\bar{N}'$ is the direction cosine of the principal ray of the extra-axial pincel $\bar{E}'\,\bar{Q}'$. Thus, the intensity at $Q'$, i.e. the point-spread function (PSF) at $(x',h')$, is given by

$$G(x',h') = |U_{Q'}|^2 = \left(\frac{1}{l\bar{N}'\,\bar{R}'}\right)^2 |F(x',h')|^2 \tag{3-6}$$

or, neglecting the constant factor

$$G(x',h') = |F(x',h')|^2 \tag{3-7}$$

The phase factor $e(x',h')$ is only of importance in treating the images of extended objects in coherent, or partially coherent, light. As a conclusion the intensity at the point $Q'$ is given essentially by the squared modulus of the Fourier transform of the pupil function $f(X',Y')$.

It is convenient in order to take advantage of the rotational symmetry of the system and for the sake of precision to change the rectangular coordinates at the exit pupil and at the image planes into polar coordinates. Then the $(X',Y')$

and the $(x', h')$ coordinates are substituted respectively by the polar notation $(r, f)$ and $(r, y)$, and consequently the diffraction integral in Eq. (3-5) changes into

$$F(r,y) = \int_0^1 \int_0^{2p} f(r,f) \exp\left[\frac{i2pr r \cos(f-y)}{lR'}\right] r dr df \qquad (3\text{-}8)$$

where the pupil function is also expressed in polar coordinates $f(r, f)$ and the maximum radius of the exit pupil is normalized to the unit. Thus, the PSF value at a point $(r, y)$ in the image plane is given by

$$G(r,y) = |F(r,y)|^2 \qquad (3\text{-}9)$$

In Eq. (3-8) $f(r, f)$ is the complex amplitude on the reference sphere that in Eq. (3-2) was given in cartesian coordinates. When Eq. (3-2) is written in polar coordinates the wave aberration is expressed as $W(r, f)$ and $t(r, f)$ is the amplitude transmittance of the system. Therefore, the PSF of an optical system depends, besides the pupil size, on the wave aberration and on the amplitude transmission of the system. The wave aberration can be written in a polynomial expansion [Hop50] as

$$W(r,f) = \sum_m \sum_n W_{mn} r^m \cos^n f \qquad (3\text{-}10)$$

If we are dealing with rotationally symmetric optical systems and with object point on axis, then, the dependence with $f$ dissappears and only even terms ($r^m$) remain. In this case the wave aberration polynomial simplifies as

$$W(r,f) = W_{20} r^2 + W_{40} r^4 + W_{60} r^6 + \ldots \qquad (3\text{-}11)$$

The term $W_{20} r^2$ expresses a defocus aberration, let us say, we are evaluating the PSF in a plane that is not the paraxial image plane. Thus, to evaluate the PSF in different planes the coefficient $W_{20}$ has to be changed. The rest of the terms in Eq. (3-11) correspond to spherical aberrations of different orders.

As we have mentioned, the PSF not only depends on the wave aberration $W(r,f)$ but also on the transmittance $t(r,f)$ of the system. As a consequence, we can change the response of the optical system by introducing non-uniform transmission filters. In the case of systems with rotational symmetry and with a smooth behavior at the origin, the amplitude transmission can be written as

$$t(r,f) = A_{00} + A_{20}r^2 + A_{40}r^4 + A_{60}r^6 + ... \qquad (3\text{-}12)$$

By changing the amplitude transmission we can modify different characteristics of the PSF (apodization, hyperresolution) and the behavior along the axis (increase of the depth of focus, multifoci) [She88, Yzu90].

Analytical expressions for the distributions of amplitude and intensity on the point spread function (PSF) are obtained only for some residual aberrations and some mathematical functions for the filter. For the general case, an accurate numerical method to evaluate the PSF must be developed. We use the numerical method developed by Hopkins and Yzuel [Hop70], with the improvements added by Yzuel and Arlegui [Yzu80] and by Yzuel and Calvo [Yzu83]. Following their numerical method, to compute the diffraction integral in Eq. (3-8) the pupil is divided into area elements, and the integral becomes a finite sum of integrals over each element. The amplitude function and the phase function, are developed in series around the element central point and first order terms are considered. The integral over each area element is obtained analytically.

In this thesis we deal with aberration-free optical systems, with object point on axis. We modify the PSF of the optical system by the addition of non-uniform transmission filters on the exit pupil.

## 3.2 Some specific non-uniform transmission pupils

Non-uniform amplitude transmission filters can be used to modify the response of optical systems [Mil86,Chu88,Cam89]. Different filter designs can

produce apodization or hyperresolution in either the transverse plane [Chu88,Cam89] or along the axis [Cam89,Yzu90]. We note that in general non-uniform transmission filters, independently of their behavior, are referred as apodizers. In this thesis, we concentrate on four specific non-uniform transmission filters located on the exit pupil of the optical system, that have been numerically studied by Yzuel *et al.* [Yzu90]. Our motivation to choose these four filters has been to be able to show a complete overview of the interesting possibilities that non-uniform transmission filters may offer in the design of optical systems. Their amplitude transmissions $t(r)$, as a function of the normalized radius $r$ in the plane of the filter, are as follows:

- $t(r) = 6.75r^2 - 13.5r^4 + 6.75r^6$. It is an axial apodizing filter that has been previously proposed and studied by Yzuel *et al.* [Yzu90] with polychromatic illumination. This filter increases the depth of focus (DOF) for the optical system and decreases the oscillations in the intensity in the axial direction.

- $t(r) = 1 - 4r^2 + 4r^4$. It is an axial hyperresolving filter. This filter decreases the depth of focus, and increases the intensity of the secondary maxima in the axial direction as shown in [Yzu90]. Therefore, we consider these axial hyperresolving filters as multifoci filters.

- $t(r) = 1 - r^2$. It is a transverse apodizing filter. It decreases the height of the sidelobes in the best image plane (BIP), and increases the width of the central maximum in the best image plane.

- $t(r) = r^2$. It is a transverse hyperresolving filter. This filter decreases the width of the central maximum in the BIP, then achieving hyperresolution in comparison with the clear aperture system. The intensity in the sidelobes is increased.

The profiles $t(r)$ for the different filters are shown in Figure 3.2 as a function of the normalized radial coordinate $r$ in the plane of the filter. The value

*r=1* corresponds to the maximum radius of the pupil. Together with the four filters we also display the clear aperture (uniform transmission filter). We note that in this thesis we consider that the system does not present any aberrations. We will see that this assumption is valid for the experimental system that we implement.

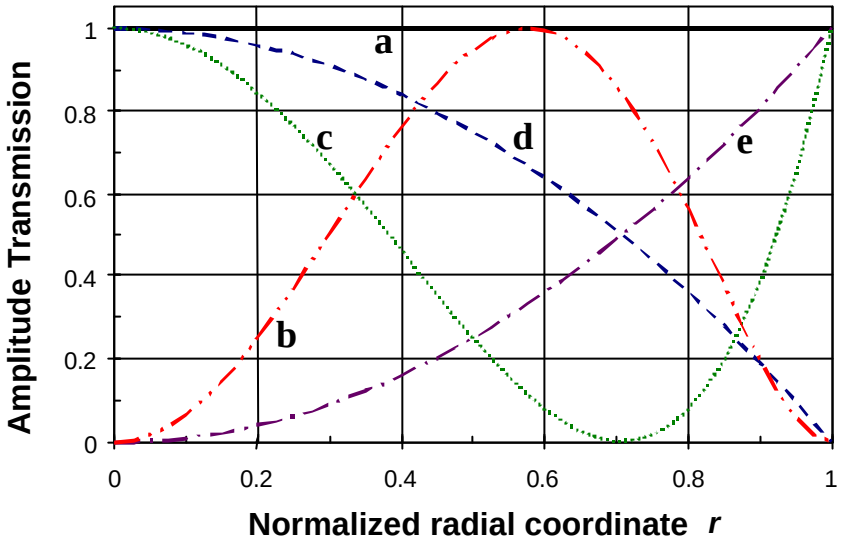


**Figure 3.2.** Amplitude pupil filter functions corresponding to **a**, uniform transmission; **b**, axial apodizing filter ($t(r) = 6.75r^2 - 13.5r^4 + 6.75r^6$); **c**, axial hyperresolving filter ($t(r) = 1 - 4r^2 + 4r^2$); **d**, transverse apodizing filter ($t(r) = 1 - r^2$); **e**, transverse hyperresolving filter ($t(r) = r^2$).

Both in the numerical and in the experimental work, the calculations made with the uniform transmission pupil serve as a frame of reference to compare the results obtained with the other four filters. In this Section we show the numerical results for the intensity values along the axis, i.e. the axial response, and the intensity values in the best image plane (BIP), i.e. the transverse response, for the different filters. The axial response is given as a function of the coefficient $W_{20}$, that is related with the shift $z$ of the image plane along the axis. The transverse response is given as a function of the normalized radial coordinate $\boldsymbol{r}$ in the image plane. The connection between the coordinates $W_{20}$ and $\boldsymbol{r}$ and their corresponding scaled axial and transverse lab coordinates $z$ and $\boldsymbol{r}'$ is the following,

$$z(mm) = W_{20}\,\frac{2\,l(mm)}{NA^2} \tag{3-13}$$

$$r'(mm) = r\,\frac{l(mm)}{NA} \tag{3-14}$$

where $l$ is the wavelength of the incident light beam and $NA$ is the numerical aperture of the system, given by

$$NA = \sin a \tag{3-15}$$

where $a$ is the angle between the optical axis of the system and the ray with origin in the limit of the pupil as we show in Figure 3.3.

$$tg\,a = \frac{R_{max}}{\tilde{R}'} \tag{3-16}$$

where $R_{max}$ and $\tilde{R}'$ are expressed in Figure 3.3.

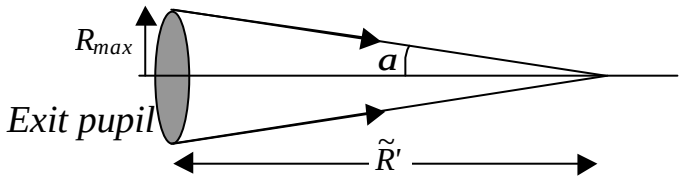


**Figure 3.3.** Characteristic parameters in order to calculate the numerical aperture ($NA$) of the optical system.

In Figure 3.4 we show the theoretical axial responses produced by the different filters. For each filter, the intensity values are normalized by its maximum intensity value, that for all the filters occurs at the BIP. In *curve* ***a*** we display the results corresponding to the clear aperture. For this case, the intensity oscillates according to a sinc-squared function as the distance $W_{20}$ to the BIP increases. *Curve* ***b*** corresponds to the axial apodizing filter. We can see that the depth of focus (DOF) increases. We also observe that the secondary maxima along the axis are eliminated. The response for the axial hyperresolving filter corresponds to *curve* ***c***. Comparing with the uniform transmission pupil, *curve* ***a***, we observe that in *curve* ***c*** the first axial minimum is closer to the BIP than in *curve* ***a***, i.e. the depth of focus has decreased. We can also see that in *curve* ***c*** the secondary maxima are highly increased in value. The filters $t(r)=1-r^2$ and $t(r)=r^2$

exhibit identical axial behavior. They correspond respectively to *curve* ***d*** and to *curve* ***e*** that are actually overlapped. We can see that the two filters have an axially apodizing behavior with no secondary maxima along the axis.

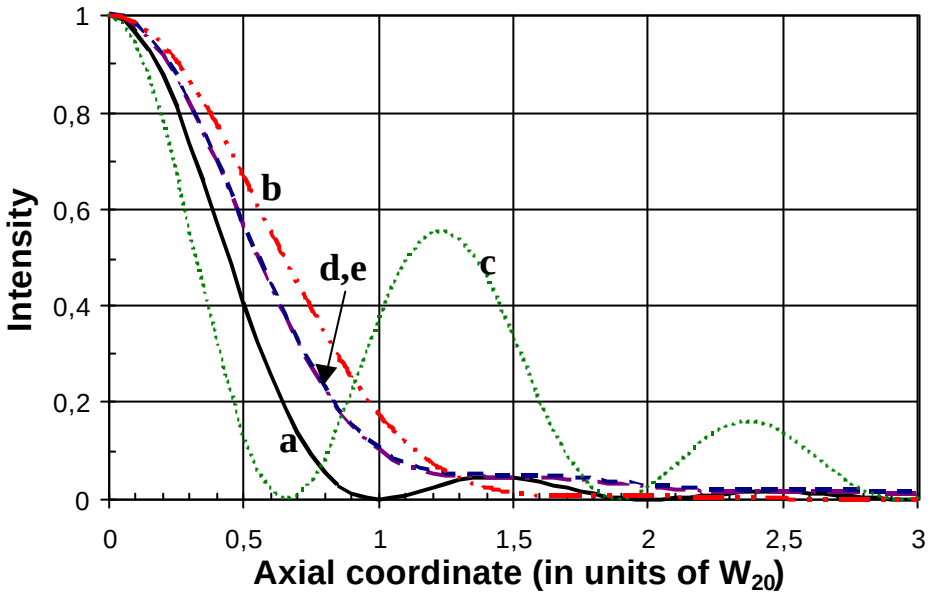


**Figure 3.4.** Theoretically calculated intensity as a function of $W_{20}$ for the amplitude pupil filters: **a**, uniform transmission; **b**, axial apodizing filter ($t(r) = 6.75r^2 - 13.5r^4 + 6.75r^6$); **c**, axial hyperresolving filter ($t(r) = 1 - 4r^2 + 4r^4$); **d**, transverse apodizing filter ($t(r) = 1 - r^2$); **e**, transverse hyperresolving filter ($t(r) = r^2$).

In Table 3.1 we resume the results shown in Figure 3.4. We give the values $W_{20}$ at which the different filters produce the maxima and minima along the axis with the corresponding intensity values at these points. For the filters that do not present maxima and minima we give the values of the intensity at the planes where the clear aperture would present the maxima and minima. The intensity values can be normalized in two different ways which we have labeled N1 and N2. In N1 the normalization is made with respect to the peak intensity value of the clear aperture at the BIP, whereas in N2 the reference value for each filter is its own intensity at the peak in the BIP. As we have seen in Figure 3.4 the clear aperture and the axial hyperresolving filter present an oscillatory behavior with maxima and minima. However, the other three filters have a monotonous decreasing behavior with the value $W_{20}$. The values displayed in Table 3.1 will be of interest when analysing the experimental results that we will show in the next

sections. Obviously, the clear aperture presents a higher transmission than the other filters. Actually, the drawback in using amplitude filters is that the light in the image plane is reduced.

| **Clear aperture** | | | |
|---|---|---|---|
| $W_{20}$ | Plane | Intensity N1 | N2 |
| 0 | BIP | 1 | 1 |
| 1 | 1rst min. | 0 | 0 |
| 1.45 | 1rst max. | 0.047 | 0.047 |
| 2 | 2nd min. | 0 | 0 |

| **Axial Apodizing** | | | |
|---|---|---|---|
| $W_{20}$ | Plane | Intensity N1 | N2 |
| 0 | BIP | 0.316 | 1 |
| 1 | --- | 0.055 | 0.17 |
| 1.45 | --- | 0.006 | 0.02 |
| 2 | --- | 0.002 | 0.007 |

| **Axial Hyperresolving** | | | |
|---|---|---|---|
| $W_{20}$ | Plane | Intensity N1 | N2 |
| 0 | BIP | 0.11 | 1 |
| 0.65 | 1rst min. | 0 | 0 |
| 1.25 | 1rst max. | 0.06 | 0.56 |
| 1.9 | 2nd min. | 0 | 0 |
| 2.35 | 2nd max. | 0.02 | 0.16 |

| **$(1-r^2)$** | | | |
|---|---|---|---|
| $W_{20}$ | Plane | Intensity N1 | N2 |
| 0 | BIP | 0.25 | 1 |
| 1 | --- | 0.025 | 0.10 |
| 1.45 | --- | 0.012 | 0.05 |
| 2 | --- | 0.006 | 0.03 |

| **$r^2$** | | | |
|---|---|---|---|
| $W_{20}$ | Plane | Intensity N1 | N2 |
| 0 | BIP | 0.25 | 1 |
| 1 | --- | 0.025 | 0.10 |
| 1.45 | --- | 0.012 | 0.05 |
| 2 | --- | 0.006 | 0.03 |

**Table 3.1.** Characteristic parameters for the numerically calculated axial response of the amplitude pupil filters.

In Figure 3.5 we show the numerical results corresponding to the transverse behavior of the filters in the BIP. As in Figure 3.4, for each filter the intensity values are normalized by its maximum intensity value, that is the N2 normalization. In comparison with *curve* ***a***, corresponding to the clear aperture, we can see the apodizing effect of the filter $t(r)=1-r^2$, *curve* ***d***, with the increased width of the central maximum. The hyperresolving effect of the filter $t(r)=r^2$, *curve* ***e***, is also evident in comparison with *curve* ***a***. The other two filters, the axial apodizing, *curve* ***b***, and the axial hyperresolving, *curve* ***c***, produce a slight increase in the width of the central maxima with respect to the clear aperture.

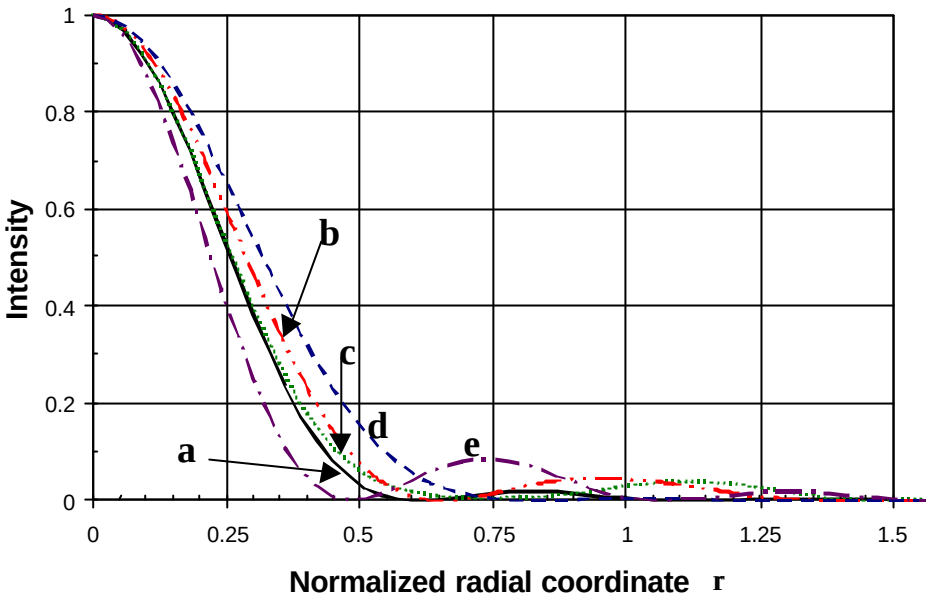


**Figure 3.5.** Numerically calculated intensity as a function of normalized transverse coordinate $r$ in the best image plane (BIP) for the amplitude pupil filters: **a**, uniform transmission; **b**, axial apodizing filter ($t(r) = 6.75r^2 - 13.5r^4 + 6.75r^6$); **c**, axial hyperresolving filter ($t(r) = 1 - 4r^2 + 4r^2$); **d**, transverse apodizing filter ($t(r) = 1 - r^2$); **e**, transverse hyperresolving filter ($t(r) = r^2$).

In Table 3.2 we express the characteristic radial positions $r$ of the maxima and minima at the BIP exhibited by the different filters. We give the intensity values at these positions according to the two normalizations N1 and N2. If we look at Table 3.2 we can see that the first minimum for the clear aperture is at $r$=0.60. Using this position as a reference, we determine if the other filters exhibit a transverse apodizing or hyperresolving performance. The bigger value is $r$=0.81 for the filter $t(r)=1-r^2$, and the smaller value is $r$=0.48 for the filter $t(r)=r^2$. This is the reason why we are calling these two filters transverse apodizing and transverse hyperresolving filters respectively. The first minimum for the axial apodizing and the axial hyperresolving filters is also bigger than $r$=0.60. Then, these two filters are also apodizing the image of the point, even though not as much as the filter $t(r)=1-r^2$. Actually, the interesting property of these two filters is mainly their axial response as we have already commented in this Section.

| Clear aperture | | | |
|---|---|---|---|
| *r* | Position | Intensity N1 | N2 |
| 0 | Center | 1 | 1 |
| 0.60 | 1rst min. | 0 | 0 |
| 0.81 | 1rst max. | 0.018 | 0.018 |

| Axial Apodizing | | | | Axial Hyperresolving | | | |
|---|---|---|---|---|---|---|---|
| *r* | Position | Intensity N1 | N2 | *r* | Position | Intensity N1 | N2 |
| 0 | Center | 0.316 | 1 | 0 | Center | 0.11 | 1 |
| 0.65 | 1rst min. | 0 | 0 | 0.75 | 1rst min. | 0 | 0 |
| 0.95 | 1rst max. | 0.015 | 0.047 | 1.11 | 1rst max. | 0.004 | 0.038 |

| $(1-r^2)$ | | | | $r^2$ | | | |
|---|---|---|---|---|---|---|---|
| *r* | Position | Intensity N1 | N2 | *r* | Position | Intensity N1 | N2 |
| 0 | Center | 0.25 | 1 | 0 | Center | 0.25 | 1 |
| 0.81 | 1rst min. | 0 | 0 | 0.48 | 1rst min. | 0 | 0 |
| 1.02 | 1rst max. | 9E-4 | 4E-3 | 0.72 | 1rst max. | 0.02 | 0.09 |

**Table 3.2.** Characteristic parameters for the numerical transverse response in the best image plane (BIP) for the amplitude pupil filters.

Amplitude pupil filters have been made using photographic emulsions with different techniques [Hee75,Mil86,She88]. However these pupil functions can be difficult and expensive to fabricate accurately and cannot be changed quickly. In this thesis we show for the first time how to program different transmissive filters using a programmable liquid crystal display that can be refreshed in real time. In Section 3.3 we show the implementation of the filters in a LCSLM working in the amplitude-only regime. In Section 3.6 we show that the programmable apodizers can also be generated on a LCSLM working in the phase-only regime.

# 3.3 Non-uniform transmission pupils onto a LCSLM in amplitude-only regime

In a recent paper [PAPER C] we demonstrated that amplitude transmitting filters can be easily implemented using a two dimensional programmable liquid crystal spatial light modulator (LCSLM) operating in the amplitude-only transmission regime. We implemented the clear aperture, the axial apodizing and the axial hyperresolving filters, and we studied their axial responses.

In [PAPER C] the LCSLM was inserted between two polarizers with their transmission axes perpendicular to the director of the LCSLM at the input and at the output faces respectively. We have studied this configuration with only polarizers both numerically and experimentally in Section 2.3.3. In Table 2.4 we can see that this configuration is actually an amplitude-mostly configuration and it does not exhibit a totally flat phase response. We note that the results in Table 2.4 correspond to the LCSLM at brightness = 50 and contrast = 100, while the work in [PAPER C] was done with the LCSLM at brightness = 50 and contrast = 85. When we decrease the value for the contrast, the range of applied voltages also decreases as it is expressed in Eq. (2-26). As a consequence the variation of the phase-shift $Dy$ is also smaller: the experimental measurements are $Dy$ = 124 and $Dy$ = 105 deg respectively for the positions brightness = 50 and contrast = 100 and for brightness = 50 and contrast = 85. Despite of this coupled variation in the phase-shift, the axial apodizing and hyperresolving profiles for the PSF obtained with the filters implemented in [PAPER C] was clearly demonstrated: we obtained an excellent agreement between the numerical and the experimental results. The big potential of this technique is that it allows the filters to be rapidly changed for modifying the response of an optical system, as the LCSLM can be refreshed at video rates.

Further research has been done on this subject and, as we have shown in Section 2.3.3, we are able to obtain an amplitude-only configuration by inserting the LCSLM between two polarizers and two wave plates, what we called the general case. As we have seen in Table 2.4, in the general case with wave plates

the coupled variation of the phase-shift $Dy$ is diminished to a value as low as 18 degrees while keeping good values for the contrast ratio $T_{max}/T_{min}$ and for the minimum transmittance value $T_{min}$. We note that the controls of the video projector are at brightness = 50 and contrast = 100. At this position the range of applied voltages is maximum, ranging from the saturation voltage to the Freedericksz voltage, what gives more relevance to the excellent values achieved for the amplitude-only configuration.

Once we can assure that we work with an amplitude-only configuration, our goal has been to perform not only a qualitative but also a quantitative study of the amplitude filters implemented on the LCSLM. In the present Section we demonstrate that we obtain a very good quantitative agreement between the numerical and the experimental results. We display and study the clear aperture and the axial hyperresolving filters. We have also implemented two new filters with respect to the ones implemented in [PAPER C]: the transverse apodizing and the transverse hyperresolving filters. With these two filters, whose interesting properties are exhibited at the BIP, we complete the study started in [PAPER C], where we implemented the axial apodizing and axial hyperresolving filters, whose interesting properties are exhibited along the optical axis.

In Table 2.4 the values to position the transmission axes of the polarizers and the slow axes of the wave plates are written. This configuration was optimized for the 458 nm wavelength of the $Ar^+$ laser. At this wavelength the retardances of the wave plates are $2f_1 = 125$ degrees and $2f_2 = 94.5$ degrees. In Figure 2.32(a) and Figure 2.32(b) we show the intensity transmission and the phase-shift curves respectively. In Figure 2.33 the complex amplitude transmittance for this configuration is plotted on the complex plane.

We implement the non-uniform transmission filters, whose performance was numerically demonstrated in the previous Section, displayed on the LCSLM. The aperture of the filter is acting as the limiting aperture of the system and the exit pupil coincides with the position of the LCSLM.

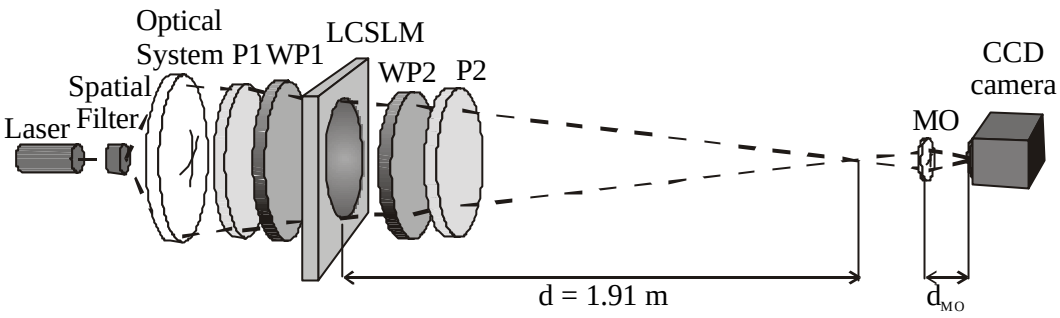


**Figure 3.6.** Scheme of the optical set-up for amplitude apodizers.

The scheme for the experimental set-up is presented in Figure 3.6. The experimental system is very simple. Light from an $Ar^+$ laser with a wavelength of 458 nm is expanded and an optical system is responsible for the convergence of the light beam. The LCSLM is inserted between the two polarizers and the two wave plates as we have already mentioned. The LCLSM is the same as the one we have characterized along Chapter 2. The aperture of the filter on the LCSLM has a diameter of 408 pixels. Taking into account the pixel spacing of 41.3 μm, the radius of the aperture is 8.4252 mm. The focused pencil converges at a distance *d* = 1.91 meters with respect to the exit pupil. The PSF is magnified using a microscope objective and imaged onto a CCD camera. In order to examine various defocus planes, the distance $d_{MO}$ between the microscope objective *MO* and detector is fixed and the entire objective/detector system is translated. Therefore, the images captured at the different defocus planes have the same magnification factor. The image onto the CCD camera is captured by means of a frame-grabber in a computer. The frame-grabber quantizes the signal from the CCD camera into 256 levels. Normally this is enough to record an accurate information about the intensity distribution in the corresponding plane. However, at certain planes we have to capture images with very low levels of light. The images we register at these planes use a small fraction of the 256 possible quantization levels, and as a consequence the recorded intensity profile is not so accurate.

The pixel structure of the SLM causes replica copies of the focus spot. These multiple orders are modulated by the sinc-squared function due to the diffraction of each pixel. The fill factor, that is the ratio of the clear aperture area

of the pixel divided by the pixel area, influences the total transmitted light and the distribution of the light among these replicas. In our set-up the microscope objective also serves as a spatial filter to eliminate these higher order diffracted images caused by the pixel structure of the LCSLM.

The transmission value for the panel is controlled by sending a voltage signal to each pixel of the LCSLM from a VGA graphic card in a computer. The graphic card sends gray scale levels (GSL) ranging from 0 to 255. Using the intensity transmission curve in Figure 2.32(a) a calibration look-up table of amplitude transmittance *t* versus GSL is formulated.

We have used Eq. (3-15) to calculate the numerical aperture of the optical system obtaining *NA = 0.0044*. In this thesis we are actually dealing with low numerical aperture optical systems. From Eq. (3-13) and Eq. (3-14) we calculate the axial and the transverse scale factors that relate the coordinates $W_{20}$ and $\boldsymbol{r}$ with their corresponding lab coordinates *z* and $\boldsymbol{r}$', obtaining:

- Axial scale factor (in mm): $\dfrac{2\boldsymbol{l}(mm)}{NA^2} = 47.1\,mm$

- Transverse scale factor (in μm): $\dfrac{\boldsymbol{l}(\boldsymbol{m}m)}{NA} = 104\ \boldsymbol{m}m$

Then, we proceed to capture the images of the characteristic axial planes for the different amplitude filters and for the clear aperture (uniform transmission). In general we are interested in capturing the transversal image (PSF) in the axial maxima and minima planes. The procedure we follow to capture these images and the measurements we carry out on them are:

1. First of all, we scale the numerical axial coordinate for the characteristic axial planes to the lab coordinate in millimeters using the axial scale factor already calculated. For convenience, we locate the origin of the axial coordinates at the best image plane (BIP).

2. We position the system objective/detector at the predicted axial position. Then, we verify that this position is actually an axial maximum or minimum as predicted. For low numerical aperture systems, we know theoretically that the intensity along the axis is symmetrical with respect to the BIP. We experimentally verify this symmetry.
3. We capture the images at the predicted distances. They are the experimental images that we show in the thesis. On these images we perform different kind of measurements that will allow us to compare the experimental values with the numerical predictions.
4. In all the images that we capture we measure the intensity (in GSL) in the intersection point between the optical axis and the image plane.
5. On the image corresponding to the BIP, we measure the radial distance (in pixels) of the different transverse minima and maxima with respect to the center of the image, and we measure the corresponding intensity value (in GSL) at these points.
6. We need to translate the experimental radial distance in pixels of the image into their value in micrometers in the lab. For doing so, we capture the image of a diffraction grating whose period is known.
7. We also need to scale the predicted radial distances for the transverse maxima and minima into their corresponding lab value in micrometers: we use the transverse scale factor already calculated.

This is the procedure we have followed both for the experimental images that we show in this Section and for the ones that we show in Section 3.5 and Section 3.6.

First of all, we show in Figure 3.7 the images captured for the clear aperture. The images correspond to the best image plane (BIP), Figure 3.7(a), the first axial minimum, Figure 3.7(b), and the first secondary axial maximum, Figure 3.7(c). The BIP position is taken as the origin for the axial lab coordinate. Under the figures we indicate the corresponding axial position in millimeters. We also

provide on the figures the equivalent transverse scale in microns for the radial distances. The images were captured under identical conditions of illumination in order to measure the relative values of intensity between them. Nevertheless, we note that in Figure 3.7 the images have been digitally saturated to show the sidelobes. We can see that the images keep a good rotational symmetry.

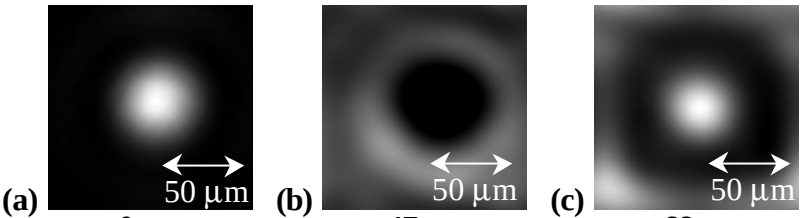


**Figure 3.7.** Experimental images of the intensity distribution for the clear aperture at the following planes. (a) BIP; (b) First axial minimum; (c) First secondary axial maximum.

| **Clear aperture (axial response)** | | | |
|---|---|---|---|
| Plane | *z (mm)* | Intensity N2 (theory) | Intensity N2 (exper.) |
| BIP | 0 | 1 | 1 |
| $1^{rst}$ min. | 47 | 0 | 0 |
| $1^{rst}$ max. | 68 | 0.05 | 0.10 |

**Table 3.3.** Comparison between the numerical and the experimental results for the intensity values at the characteristic axial planes for the clear aperture.

In Table 3.3 we show the comparison between the numerical predictions and the experimental results for the intensity measurements performed on the images captured at the axial planes shown in Figure 3.7. We show the intensity values normalized with respect to the intensity maximum at the BIP (N2 normalization ). First, we want to remark that the experimental maxima and minima planes coincide with the predicted positions. This is actually an excellent result that, as we will see along the different Sections, we obtain with the other filters as well. We want to quote that the three images in Figure 3.7 have been taken under identical illumination conditions and this produces a very low dynamic range (about 20 quantization levels) for the first secondary maximum image. This limits the accuracy in the measurement of the peak value at this plane. As a whole, we can say that the experimental intensity values are close to the numerical ones.

In Table 3.4 we compare the radial distances of the maxima and minima and the intensity values at these positions for the BIP image. In this case, both the agreement between the numerical and the experimental radial distances and the agreement between the intensity values is very good.

| **Clear aperture (transverse response)** | | | | |
|---|---|---|---|---|
| Position | *r' (mm)* (theory) | Intensity N2 (theory) | *r' (mm)* (exper.) | Intensity N2 (exper.) |
| Center | 0 | 1 | 0 | 1 |
| 1$^{rst}$ min. | 62.3 | 0 | 65.8 | 0 |
| 1$^{rst}$ max. | 84.1 | 0.02 | 92.1 | 0.02 |

**Table 3.4.** Comparison between the numerical and the experimental results for the intensity values at the characteristic transverse positions at the BIP for the clear aperture.

In the following we will study the axial hyperresolving filter. In Figure 3.8 we show the images captured for this filter at its characteristic axial positions.

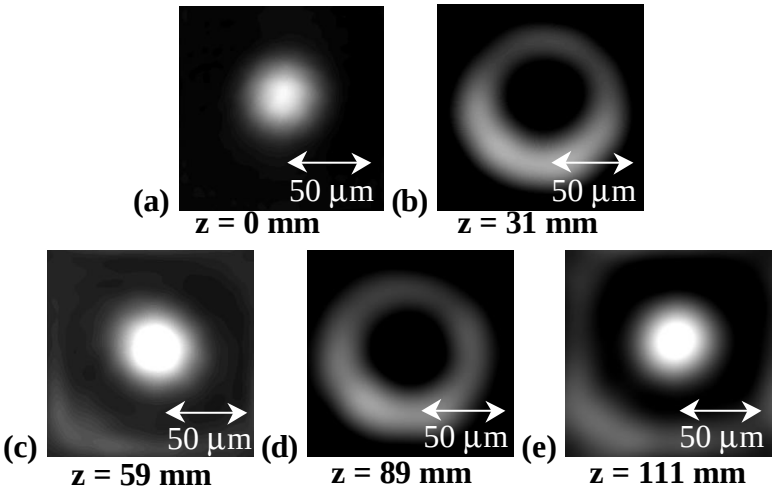


**Figure 3.8.** Experimental measurements of the response for the amplitude filter $t(r) = 1 - 4r^2 + 4r^4$ at the following planes. (a) BIP; (b) First axial minimum; (c) First secondary maximum; (d) Second axial minimum; (e) Second axial maximum.

The images in Figure 3.8 have been taken under identical conditions of illumination in order to compare their respective intensity values. As in Figure 3.7, the images in Figure 3.8 have been digitally saturated in order to show the sidelobes. We appreciate a rather good rotational symmetry in all the axial planes. The slight lack of rotational symmetry can be due to minor misalignments in the experimental set-up, and to the residual aberrations introduced by the different

plane-parallel surfaces existing in the set-up, mainly polarizers and wave plates. We note that the LCSLM that we are using is almost free of aberrations and allows us to obtain diffraction limited images.

For the axial hyperresolving filter the interesting response is the axial response. In Table 3.5 we show the measurements done at the center of the different planes. The multifoci behavior is clearly demonstrated by the high values for the intensity at the secondary maxima. We also remark that the different minima and maxima planes coincide with the numerical prediction.

| **Axial hyperresolving filter (axial response)** | | | |
|---|---|---|---|
| Plane | *z (mm)* | Intensity N2 (theory) | Intensity N2 (exper.) |
| BIP | 0 | 1 | 1 |
| 1$^{rst}$ min. | 31 | 0 | 0 |
| 1$^{rst}$ max. | 59 | 0.56 | 0.31 |
| 2$^{nd}$ min. | 89 | 0 | 0 |
| 2$^{nd}$ max. | 111 | 0.16 | 0.10 |

**Table 3.5.** Comparison between the numerical and the experimental results for the intensity values at the characteristic axial planes for the axial hyperresolving filter.

Now we study the filters $t(r) = 1 - r^2$ and $t(r) = r^2$. Along the optical axis we have experimentally verified that both filters provide approximately the same values as theoretically predicted. Actually the interesting properties of these filters are at the BIP. In Figure 3.9 we show the BIP images captured for both filters. The images have been digitally saturated in order to show the sidelobes. In Figure 3.9(a) we have combined the focused spots from the filter $t(r) = 1 - r^2$ (upper half) and from the filter $t(r) = r^2$ (lower half). We can clearly appreciate the larger width of the central maximum for the filter $t(r) = 1 - r^2$ with respect to the filter $t(r) = r^2$. We can also distinguish the radial sidelobe for the filter $t(r) = r^2$. These features are indicative of the relative apodizing and hyperresolving properties at the BIP between the two filters $t(r) = 1 - r^2$ and $t(r) = r^2$. On Figure 3.9(b) and on Figure 3.9(c) we present again the images at the BIP for both filters, where we indicate their respective peak intensity values (in gray level). We can see that the peak intensity is exactly equal in both images. This is actually what the numerical results predict. On the images we also show the equivalent transverse scale in

microns for the radial distances. We use this scale to measure the position of the maxima and minima at the BIP.

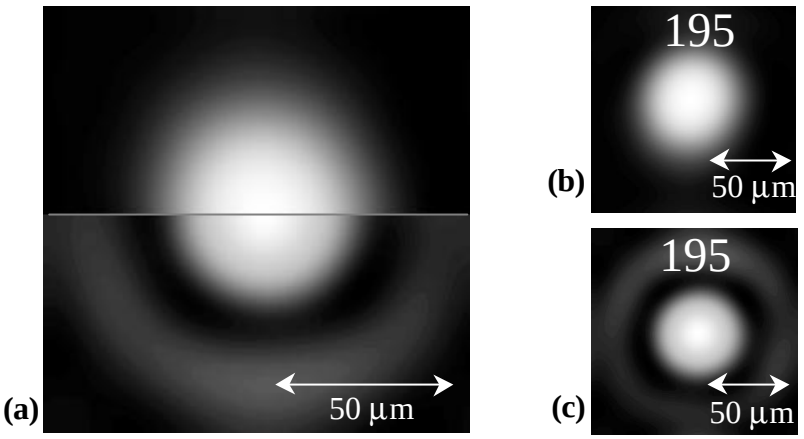


**Figure 3.9.** Experimental PSF images at the BIP of the intensity of the focused spot. (a) Combination of saturated images (upper half, filter $t(r) = 1 - r^2$; lower half, filter $t(r) = r^2$). (b) For filter $t(r) = 1 - r^2$. (c) For filter $t(r) = r^2$.

In Table 3.6 we resume the different measurements carried out on the images in Figure 3.9. We compare these measurements with the numerical predictions. We can see that once again, the agreement between the numerical and the experimental values is very good. It is also important to compare the results for these two filters with respect to the clear aperture results in Table 3.4. We see that the first transverse minimum for the clear aperture, at $\boldsymbol{r}'$=65.8 μm, is located at an intermediate position between the corresponding distances $\boldsymbol{r}'$=88.3 μm for the filter $t(r) = 1 - r^2$, and $\boldsymbol{r}'$=54.3 μm for the filter $t(r) = r^2$. Therefore, the filter $t(r) = 1 - r^2$ apodizes the PSF while the filter $t(r) = r^2$ is clearly hyperresolving. As a final comment, we note that we could not measure the position for the first secondary maximum at the image for the filter $t(r) = 1 - r^2$ because it is out of the area of the sensor of the CCD camera. We can conclude after this quantitative analysis that we are able to produce transverse apodizing and hyperresolving performances at the BIP using the LCSLM.

| $t(r) = 1 - r^2$ (transverse response) | | | | |
|---|---|---|---|---|
| Position | *r' (mm)* (theory) | Intensity N2 (theory) | *r' (mm)* (exper.) | Intensity N2 (exper.) |
| Center | 0 | 1 | 0 | 1 |
| 1rst min. | 84.1 | 0 | 88.3 | 0 |
| 1rst max. | 105.9 | 0.004 | --- | --- |

| $t(r) = r^2$ (transverse response) | | | | |
|---|---|---|---|---|
| Position | *r' (mm)* (theory) | Intensity N2 (theory) | *r' (mm)* (exper.) | Intensity N2 (exper.) |
| Center | 0 | 1 | 0 | 1 |
| 1rst min. | 49.8 | 0 | 54.3 | 0 |
| 1rst max. | 74.7 | 0.08 | 79.9 | 0.07 |

**Table 3.6.** Comparison between the numerical and the experimental results for the intensity values at the characteristic transverse positions at the BIP for the filters: (a) $t(r) = 1 - r^2$; (b) $t(r) = r^2$.

In conclusion, we report the use of an amplitude transmitting LCSLM for introducing programmable apodizing filters into optical systems. Experimental results for the axial and the transverse positions of the characteristic minima and maxima for the different filters are in excellent agreement with theoretical predictions. In general, the agreement is also very good between the numerical and the experimental intensity values shown in the different tables. After the quantitative analysis performed in this Section we can assure that the apodizing and hyperresolving properties of the different filters have been clearly demonstrated using the LCSLM. The technique is easy to implement and should allow experimental results for various transmissive filters to be obtained easily. The big potential of this technique is that the video rate refreshment of the LCSLM allows the filters to be rapidly changed for modifying the PSF of an optical system.

## 3.4 Encoding amplitude information onto a focusing element

A very powerful and attractive property of diffractive optical elements (DOEs) is the possibility to combine different functions in the same DOE. In this

thesis we present a proposal which takes advantage of this possibility. Our interest is to combine the PSF transformation property of non-uniform transmission filters with the focusing property of lenses. This combination leads to a new device, the programmable focusing apodizer, whose focal length and whose apodizing or hyperresolving action on the image formation behavior of the system can both be changed in real time.

In order to generate programmable focusing apodizers with the LCSLM we have to take into account several considerations that we develop in Section 3.4 and 3.5. The first point, that we develop in this Section, deals with the need to codify complex amplitude information into a media with modulation constraints as the LCSLM. The second point, developed in Section 3.5, deals with an effect associated with the pixelated nature of the LCSLM that modifies the performance of lenses, and as a consequence the performance of the programmable focusing apodizers as well.

The first point to consider is that we want to combine an amplitude-only element, the non-uniform transmission filter, with a phase-only element, the lens. We have to implement a complex amplitude transmittance onto the LCSLM and we should be able to control independently the amplitude and the phase modulations. As we have already seen along Chapter 2, the amplitude and the phase are coupled magnitudes in the LCSLMs. In fact, there is no SLM device that can simultaneously provide independent amplitude and phase modulation. This limitation is important in different fields of optical information processing and in diffractive optics where elements with a complex amplitude transmittance are needed. This is the motivation for a variety of works where different strategies are designed to implement complex amplitude information on media with a restricted modulation capability. One of the earliest methods was described by Kirk and Jones [Kir71]. A continuous (low-frequency) surface-relief profile that controls the phase is superimposed with an amplitude-modulated (high-frequency) sinusoidal carrier grating that deflects a controlled amount of light into higher carrier orders and, therefore, simulates an absorbing layer. This technique is

extremely difficult to implement, particularly with SLMs, because of the need for a high-frequency carrier. In an alternate approach [Gre92,Gon96] two LCSLMs were combined to achieve total amplitude and phase operation. This is difficult to implement experimentally. Moreover, it is more interesting to achieve amplitude and phase information with a single SLM. Davis *et al.* [Dav99d] performed a good revision of the different methods available to implement complex amplitude information on media with a restricted modulation capability. In this paper [Dav99d] they proposed a new procedure which is suitable for low resolution media as the LCSLMs. We note that the highest spatial frequency that can be displayed in a LCSLM is about 30 lines/mm. This is the method that we have used in the work performed in this thesis to encode the programmable focusing apodizers. In what follows we will explain this codification method.

The programmable focusing apodizers are generated on the LCSLM in the phase-only regime. This is the suitable regime to display the lens, as it is a phase encoded element. In order to achieve the lens and the non-uniform amplitude filter displayed in the same LCSLM, in the phase-only regime, in [PAPER E] we extended to a quadratic phase carrier the method proposed by Davis *et al.* [Dav99d] with a linear phase carrier.

The method is based on the encoding of an arbitrary complex function by means of an adequate phase function. In Ref. [Dav99d] the proposal was to add a linear phase grating to a phase-only filter for pattern recognition. The intuitive idea of this method can be viewed in Figure 3.10 where a blazed phase grating with different values for the phase depth is shown. If the phase depth equals $2\pi$ radians, Figure 3.10(a), all the incident light is diffracted into the first diffraction order. In the case the phase depth is $\pi$ radians, Figure 3.10(b), an equal percentage of 40.5 % of the incident light is distributed into the first and the zero diffraction orders and the remaining 19 % is sent to the other orders. If the phase depth were zero, then all the incident light would be sent into the zero order. Thus, if we vary the phase depth along the blazed grating, we can obtain a spatial modulation of the light diffracted to the zero order and to the first order. For example, in Figure

3.10(c), the phase depth is $2\pi$ at the center of the grating and gradually diminishes to zero at the edges. Therefore the center of the grating is sending all the light into the first diffraction order while the edges send the light into the zero order. The complementary effect would be obtained with the profile in Figure 3.10(d).

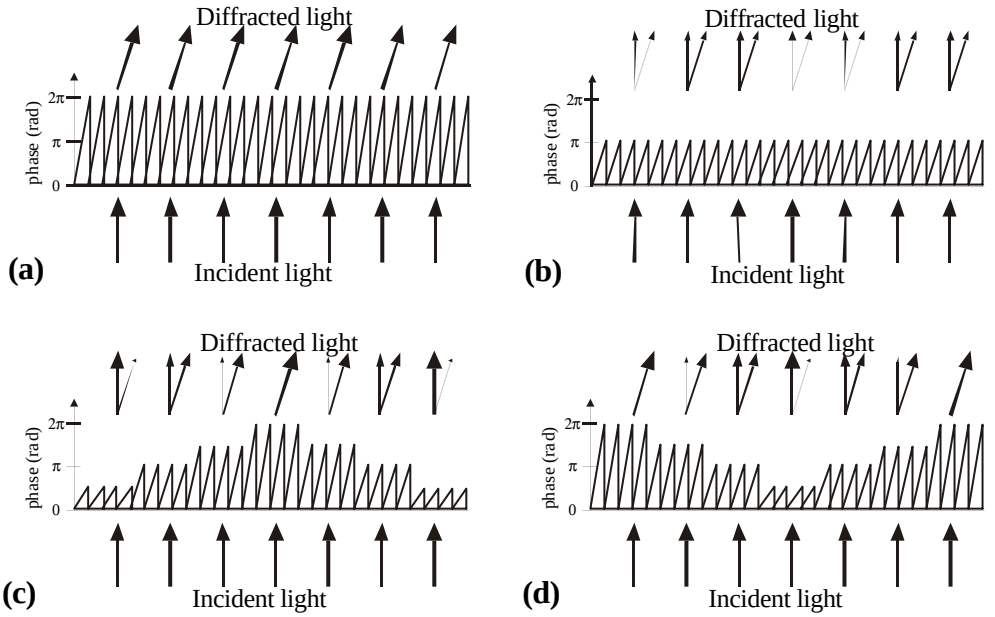


**Figure 3.10.** Blazed phase grating with different phase depth. (a) $2\pi$ radians; (b) $\pi$ radians; (c) Modulated with $2\pi$ radians at the center; (d) Modulated with $2\pi$ radians at the edges.

With the blazed phase grating we have shown that a phase element is able to encode amplitude transmission information to spatially modulate a beam of light. With the proper design of the phase depth across the phase grating we can obtain a specific response in the desired diffraction order.

In this thesis we concentrate on a different geometry, that was proposed in [PAPER E]. We consider a quadratic phase carrier instead of the linear phase carrier considered in [Dav99d]. By means of the quadratic phase carrier we can display the complex amplitude information represented by the combination of the amplitude filter and the lens in a single LCSLM working in the phase-only mode. Let us consider the general case of a complex amplitude filter. We can represent the complex transmittance of this filter as a function $T(x,y) = M(x,y)\exp[i\Phi(x,y)]$, where $|M(x,y)| \le 1$ represents the amplitude

information and $-\pi \le \Phi \le \pi$ is the phase information. In the case of amplitude-only transmission filters we simply have to substitute $\Phi = 0$.

Let $Z^*(x,y)$ be the quadratic phase introduced by a lens with focal $f$, illuminated with a plane wave of wavelength $\lambda$,

$$Z^*(x,y) = exp\left[-i\frac{\pi}{\lambda f}\left(x^2+y^2\right)\right] \tag{3-17}$$

Thus, to display both the filter and the lens on the same LCSLM in phase-only regime, we have to phase encode the next complex function

$$G(x,y) = T(x,y)Z^*(x,y) = T(x,y)\,exp\left[-i\frac{\pi}{\lambda f}\left(x^2+y^2\right)\right] \tag{3-18}$$

As in Ref. [Dav99d], we define the phase function $G'(M',\psi) = exp[iM'\psi]$, with $|M'| \le 1$ and $-\pi \le \psi \le \pi$, where $\psi = \Phi(x,y) - \frac{\pi(x^2+y^2)}{\lambda f}$. Then, we define the periodical extension $G''(M', \psi)$ of this function by repeating it in the range $-\infty \le \psi \le \infty$. The Fourier expansion of this periodical function will be

$$G''(M',\psi) = \sum_{n=-\infty}^{n=\infty} G_n \exp[i n \psi] \tag{3-19}$$

where $G_n = sinc(M' - n)$, with the usual definition $sinc(x) = sin(\pi x)/(\pi x)$. We can rewrite $G''$ in terms of $x$ and $y$

$$G''(x,y) = \sum_{n=-\infty}^{\infty} sinc[M'(x,y) - n]\exp\left[i n\left(\Phi(x,y) - \frac{\pi(x^2+y^2)}{\lambda f}\right)\right] \tag{3-20}$$

We consider that a plane wave with wavelength $\lambda$ illuminates a LCSLM where this transmission has been displayed. According to the Fresnel diffraction theory, the resulting electric field $U'(u,v)$ on the plane $(u,v)$ placed at a distance $f$ of the plane $(x,y)$ will be proportional to

$$U'(u,v) \propto \exp\left[\frac{i\pi(u^2+v^2)}{\lambda f}\right]\int_{-\infty}^{\infty}\int_{-\infty}^{\infty}\sum_{n=-\infty}^{\infty} sinc\left[M'(x,y)-n\right]$$
$$\exp\left[i n\left(\Phi(x,y)-\frac{\pi(x^2+y^2)}{\lambda f}\right)\right]\exp\left[\frac{i\pi(x^2+y^2)}{\lambda f}\right]\exp\left[\frac{-i2\pi(ux+vy)}{\lambda f}\right]dxdy \quad (3\text{-}21)$$

The sum over the *n*-indices in Eq. (3-21) can be taken out of the integral symbol. Thus, the resulting amplitude distribution *U´(u,v)* is equal to the addition of the Fresnel diffraction produced by each of the *n*-terms. For the term $n=1$ we see that the quadratic phase functions inside the integral cancel. The contribution of the term $n=1$ to the amplitude *U´(u,v)* will be the Fourier transform of $sinc\left[M'(x,y)-1\right]\exp\left[i\Phi(x,y)\right]$. Additionally, we can choose the function $M'(x,y)$ so that $sinc\left[M'(x,y)-1\right]=M(x,y)$. In this way, the term $n=1$ produces on the plane (*u,v*) the Fourier transform of the amplitude function $M(x,y)$ that we wanted to encode onto the Fresnel lens. Thus, we have demonstrated that the term $n=1$ is carrying the desired amplitude-only information $M(x,y)$.

For the other terms ($n \neq 1$), the quadratic phase $\exp\left[i n\pi\left(x^2+y^2\right)/\lambda f\right]$ in Eq. (3-21) is not compensated. In general, the phase of the *n*-term can be thought as produced by a lens with a focal length *f/n*. These terms will appear defocused and their contribution will be almost a constant on the plane (*u,v*). Moreover, the intensities of these defocused terms are governed by the function $sinc\left[M'(x,y)-n\right]$ and because $0 \le M'(x,y) \le 1$ the main contribution is given by the zero order term. Even for this term the resulting intensity will be lower than the contribution given by the term $n=1$. In conclusion, the resulting intensity in the plane (*u,v*) will be the Fourier transform of the function that we have encoded (given by the term $n=1$) plus a low background noise (given by the other terms).

In an example given in [PAPER E], we have evaluated the signal to noise ratio (SNR) of the intensity when an apodizing function *M(x,y)* is encoded. We have chosen $M(x,y)=1-\frac{x^2+y^2}{R_{max}^{\ 2}}$, with $R_{max}$ the lens radius. In this case the

SNR was 1:0.005. This high value shows that the contribution of the terms $n \neq 1$ can be neglected.

Concluding, we have demonstrated a method that is able to encode complex amplitude information, in particular amplitude-only information, onto a phase-only medium. When we encode an amplitude-only transmission function onto the quadratic phase function corresponding to the lens, the contribution of the first order term is enhanced at the focal plane of the lens function while the terms where $n \neq 1$ are defocused. Therefore at the focal plane of the encoded lens, the field distribution produced by the encoded function will be the Fourier transform of the desired function immersed on a very low background noise.

## 3.5 Inherent equivalent apodizing effect in pixelated Fresnel lenses

### 3.5.1 Theory

In a recent work [PAPER D] we introduced what we called the inherent equivalent apodizing effect. This is a phenomenon that is originated in devices with a pixelated structure as the LCSLMs. This effect is particularly important not only for lenses encoded onto LCSLMs but also for all focusing DOEs, such as the programmable focusing apodizers, that we show in Section 3.6. Along the present Section we introduce this effect and we show that it leads to apodization of the image produced by the lens on the LCSLM. As a consequence it distorts the response of the programmable focusing apodizers as well. We demonstrate a technique to measure and compensate for this effect.

In this Section we concentrate our attention on the generation of lenses onto the LCSLM. The results obtained can be extended to other focusing DOEs. These lenses belong to the category of the diffractive Fresnel lenses, explained in Section 1.3.2. In the case of the LCSLM it is obvious that the phase profile of the lens is sampled by the pixelated structure of the LCSLM. Furthermore, the profile

of the lens is quantized in 256 levels, corresponding to the VGA resolution of the LCSLM we are using in this thesis (Sony Model LCX012BL).

Different authors [Dav89a,Cot90,Lau98] have reported that Fresnel phase-encoded lenses can be displayed on a programmable SLM. The sampling of the Fresnel lens causes the appearance of multiple lenses when the sampling frequency is lower than the Nyquist frequency as we show in Figure 3.11. This leads to the appearance of secondary maxima in the focal plane with a loss of efficiency in the principal focus.

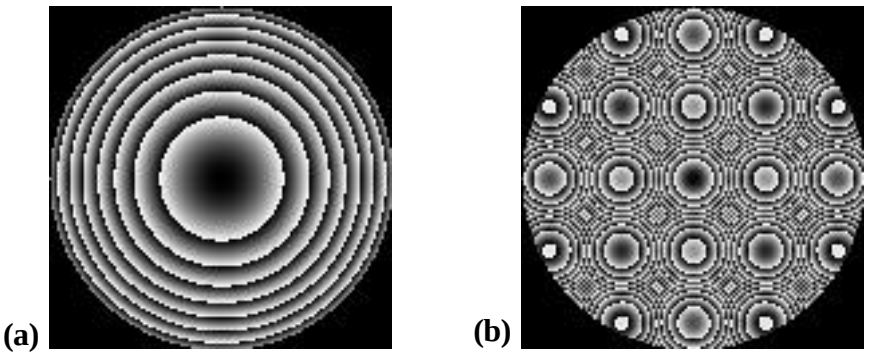


**Figure 3.11.** Fresnel lenses with different focal lengths and with the same sampling frequency. The shorter the focal length the higher the Nyquist frequency needed to sample the lens function. (a) Sampling frequency higher than the Nyquist frequency; (b) Sampling frequency lower than the Nyquist frequency and we can see the appearance of secondary lenses.

Carcolé *et al.* [Car94a,Car94b,Car95] studied theoretically low resolution Fresnel lenses and they provided some optimization procedures in order to enhance the fraction of energy that goes to the focus of the main lens. In Ref. [Car94a] Carcolé *et al.* developed a mathematical model that describes the behavior of the low resolution Fresnel lenses and they obtained expressions for the light distribution in the focal plane due to the main lens and to the secondary lenses. A very important result is that the image produced by a lens encoded onto a SLM appears to be convolved with the function that describes the pixel shape. This result leads to the apodizing effect reported by Arrizón *et al.* [Arr99]. This phenomenon is what, in [PAPER D], we have named as the inherent equivalent apodizing effect. In the paper we provide the means to measure this effect and to compensate for it.

In this Section we follow the approach by Carcolé *et al.* In the Appendix we develop an alternative theoretical approach based on the concept of diffraction efficiency. The approach in the Appendix is not as general as the one given in this Section, however, it provides an intuitive idea of the phenomenon of the inherent equivalent apodizing effect.

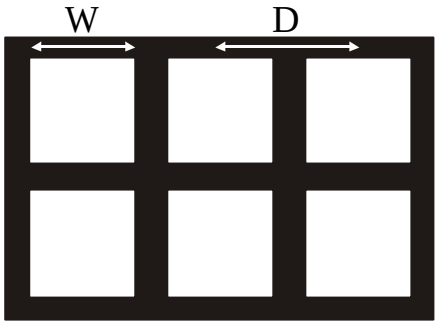


**Figure 3.12.** Pixelated structure of the LCSLM. The existence of dead areas for the electrode wires between the clear aperture of the pixels makes that the width W of the pixel is smaller than the distance D between center to center of consecutive pixels.

In order to display a converging lens we send a quadratic phase $f_Q(x,y)$ to the SLM working in the phase-only regime. This phase function is given by

$$Z^*(x,y) = exp\left[-i f_Q(x,y)\right] = exp\left[-i\frac{p}{lf}\left(x^2 + y^2\right)\right] \qquad (3\text{-}22)$$

where $f$ is the focal length. In what follows we use a one-dimensional notation for simplicity. If we encode this lens on a pixelated device having a length $L$ with pixel spacing of $D$ and pixel width of $W$ (Figure 3.12), the transmission of the SLM is

$$T(x) = \left(\left(Z^*(x)\sum_n \delta(x - nD)\right) rect\left(\frac{x}{L}\right)\right) \otimes rect\left(\frac{x}{W}\right) \qquad (3\text{-}23)$$

Here the symbol $\otimes$ represents the convolution operation. The operations we are performing in Eq. (3-23) when encoding the quadratic phase function are the following: sampling the function at distances $D$ given by the spacing of the pixels, spatially limiting because of finite extent $L$ of the SLM and convolving this sampled function by the shape of the pixel, due to the finite width $W$ of the pixel.

It is important to note that across the pixel the phase value is constant, as we observed in the stepped phase profile for the diffractive lens in Figure 1.5. We will demonstrate that this constant phase value across the pixel constitutes the origin for the inherent equivalent apodizing effect in pixelated lenses.

When the SLM is illuminated with a plane wave the amplitude distribution $U(u)$ in the focal plane of the encoded lens is given by Fresnel diffraction and can be obtained by convolving Eq. (3-23) with a quadratic diverging phase function given by *Z(x)*,

$$U(u) = \int T(x) Z(u-x) dx \tag{3-24}$$

We have to perform two convolutions in Eq. (3-23) and Eq. (3-24). By using the associative and commutative properties of the convolution function, we can write the amplitude in the focal plane as

$$U(u) = \left[ \int \left( Z^*(x) \sum_n \delta(x - nD) \right) rect\left(\frac{x}{L}\right) Z(u-x) dx \right] \otimes rect\left(\frac{u}{W}\right) \tag{3-25}$$

The amplitude in the focal plane can be evaluated by calculating first the propagation of the sampled lens (without taking into account the pixel size), and then convolving the result with the pixel shape. Apart from a constant multiplicative factor, the result is given by

$$U(u) = \left\{ exp\left( i \frac{\pi}{\lambda f} u^2 \right) \left[ sinc\left(\frac{Lu}{\lambda f}\right) \otimes \sum_n \delta\left( u - n\frac{\lambda f}{D} \right) \right] \right\} \otimes rect\left(\frac{u}{W}\right) \tag{3-26}$$

where $sinc(x) = sin(\pi x)/\pi x$. We can see that Eq. (3-26) yields a superposition of *sinc* functions having widths of $(\lambda f)/L$ and separations of $(\lambda f)/D$, as we show in Figure 3.13. The separations between the *sinc* functions are much larger than their widths because $L=ND$ where $N$ is the number of pixels in a row of the SLM. Because we are interested in evaluating the amplitude in the central zone of the focal plane, we only have to consider the contribution of the *n=0 sinc* function. In addition, the quadratic phase term in Eq. (3-26) can be neglected in the central

zone because its phase variations across the rectangle function and the central lobe of the sinc function are much less than $2\pi$ radians. In this case the amplitude in the focal plane can be written as

$$U(u) = sinc\left(\frac{Lu}{\lambda f}\right) \otimes rect\left(\frac{u}{W}\right) \tag{3-27}$$

This result shows that the shape of the focused spot will be convolved with a rectangle function having the width of the pixels in the SLM.

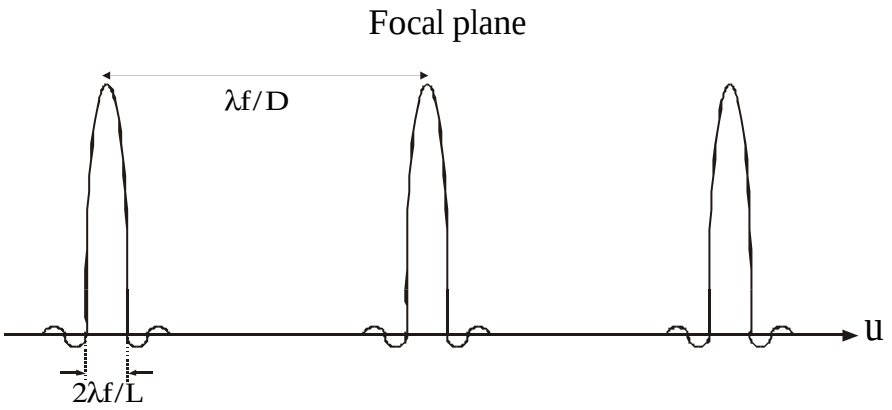


**Figure 3.13.** The separation between the different replicas due to the pixelated structure of the LCSLM is much larger than the width of the *sinc* functions.

In image formation, the point-spread function is equal to the Fourier transform of the pupil function. The PSF produced by the encoded lens is given by Eq. (3-27). Consequently, we have an effective pupil function that is equal to the inverse Fourier transform of Eq. (3-27). This pupil function is given by the product of a rectangle function of width $L$ that corresponds to the size of the SLM and a *sinc* function that corresponds to the Fourier transform of the pixel. This *sinc* function acts as a non-uniform transmission pupil $\tau(x)$. It is a transmission function whose profile decays at the edges. Thus, the *sinc* function acts as an equivalent apodizing function that is given by

$$\tau(x) = sinc\left(\frac{Wx}{\lambda f}\right) \tag{3-28}$$

The effects of this equivalent apodizing function will become more severe as the width of the pixel increases or as the focal length of the lens decreases. Taking into account that the pixel shape in the LCSLMs that we use is square and with a pixel width *W* the actual equivalent apodizing function in the two dimensions (*x*,*y*) is

$$t(x,y) = sinc\left(\frac{Wx}{\lambda f}\right) sinc\left(\frac{Wy}{\lambda f}\right) \tag{3-29}$$

At this point, we want to remark the difference existing with the case in which no lens is addressed onto the pixelated SLM and the focusing of light is produced by a refractive lens placed just behind the SLM. In this case the amplitude of the wave front behind the lens is expressed by

$$T'(x) = \left[\left(\sum_n \delta(x - nD)\ rect\left(\frac{x}{L}\right)\right) \otimes rect\left(\frac{x}{W}\right)\right] Z^*(x) \tag{3-30}$$

Note that now the phase across the pixel dimension is not constant. As we did in Eq. (3-24) the amplitude distribution in the focal plane of the lens is given by Fresnel diffraction and can be obtained by convolving Eq. (3-30) with a quadratic diverging phase function given by *Z(x)*. Apart from a constant multiplicative factor, the result is

$$U'(u) = \left\{exp\left(i\frac{\pi}{\lambda f}u^2\right)\left[sinc\left(\frac{Lf}{\lambda f}\right) \otimes \sum_n \delta\left(u - n\frac{\lambda f}{D}\right)\right]\right\} sinc\left(\frac{Wx}{\lambda f}\right) \tag{3-31}$$

where the effect of the pixel in the amplitude distribution in the focal plane is the product with the *sinc(Wx/λf)* function. The effect of the pixel is clearly different in this case with respect to the case when a lens is displayed onto the SLM (Eqs. (3-26) and (3-27)), in which we obtain in the focal plane a convolution operation with the rectangle function that expresses the shape and width of the pixel. In the case of the encoded lens in the SLM this effect can be considered as an apodization on the plane of the lens.

### 3.5.2 Calibration method with annular masks

In the present Section we demonstrate an experimental method to obtain direct measurements for the amplitude transmission profile along the aperture of the lens. These experimental data can be used to calculate the function that compensates the actual non-uniform amplitude transmission profile along the aperture of the lens.

Let us introduce the theory in which the experimental method that we present in this Section is based. We know that the amplitude $U(\mathbf{r}=0)$ in the center of the focal plane ($\mathbf{r}$ is the radial coordinate in the focal plane) of an optical system without aberrations is given by

$$U(\mathbf{r}=0)=\iint_R \mathbf{t}(r,\mathbf{f})rdrd\mathbf{f} \tag{3-32}$$

where $(r,\mathbf{f})$ are the polar coordinates in the pupil plane and $\mathbf{t}(r,\mathbf{f})$ is the amplitude transmission of the pupil. The integral is extended to the pupil region $R$. In the case of radial symmetry, the above expression becomes

$$U(\mathbf{r}=0)=2\mathbf{p}\int_R \mathbf{t}(r)rdr \tag{3-33}$$

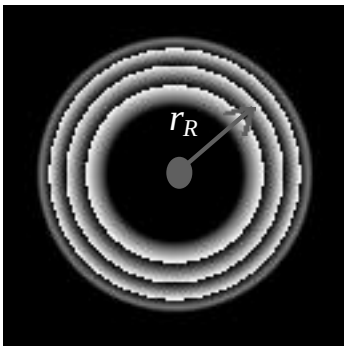


**Figure 3.14.** Annular ring with central radius $r_R$, where we can see the encoded lens.

Let us consider that we display a lens function whose clear aperture is given by a ring with central radius $r_R$. We illustrate in Figure 3.14 an annular ring of central radius $r_R$ where the encoded lens can be distinguished through the clear

area of the ring. We take the annular ring with a width small enough so that $t(r)$ is almost constant inside of the area $A$ of the ring. Then from Eq. (3-33) we obtain

$$U(r=0) = A\,t(r_R) \tag{3-34}$$

Experimentally, the magnitude that we can measure is the intensity. The modulus of the amplitude in the center of the focal plane $U(r=0)$ is given by the square root of the intensity $I(r=0)$. Thus, taking into account Eq. (3-34) we can calculate the value of $t(r_R)$ as follows

$$t(r_R) = \frac{\sqrt{I(r=0)}}{A} \tag{3-35}$$

If the apodizing effect were not present we would have that $t(r_R)=1$ independently of the central radius $r_R$ of the ring. The annular rings would yield focused intensities that are proportional to the square of the areas of the annular rings. But with the apodizing effect these intensities will be proportional to the product of the square of the area of the annular rings by the square of the apodizing function. Then, by measuring the intensities produced by annular rings centered in different radius $r_R$, we are able to deduce the inherent apodization function $t(r_R)$ along the aperture of the lens.

The basis for the experimental method we propose is to program annular rings having different central radii and areas onto the lens function. Then, we measure the focused intensity from each ring. According to Eq. (3-35), from these intensity measurements we can extract the value for the equivalent transmission $t(r_R)$ along the aperture of the pupil. For these experiments, the quadratic phase function is encoded inside the area corresponding to the transmissive part of the annular ring while a constant phase is encoded for the remaining region of the lens. We note that the annular mask has a rotational symmetry, while the theoretical apodizing function obtained in Eq. (3-29) has a cartesian symmetry due to the shape of the pixel in the LCSLM. Then, the results obtained with the annular masks have to be considered as the angular average along the region of the LCSLM in the clear area of the ring.

In what follows we describe the experimental set-up that we use to generate the Fresnel lenses on the LCSLM, and in general any phase encoded DOE. We show the set-up in Figure 3.15, where we can observe that it is very similar to the set-up used in Section 3.3, Figure 3.6, to generate the programmable apodizers on the LCSLM working in the amplitude-only regime. In the present case we are interested in displaying a phase encoded element, the Fresnel lens, thus, we need the LCLSM working in the phase-only regime. Another difference with respect to Figure 3.6 is that we do not need an external lens to form the image as the lens is displayed on the LCSLM itself.

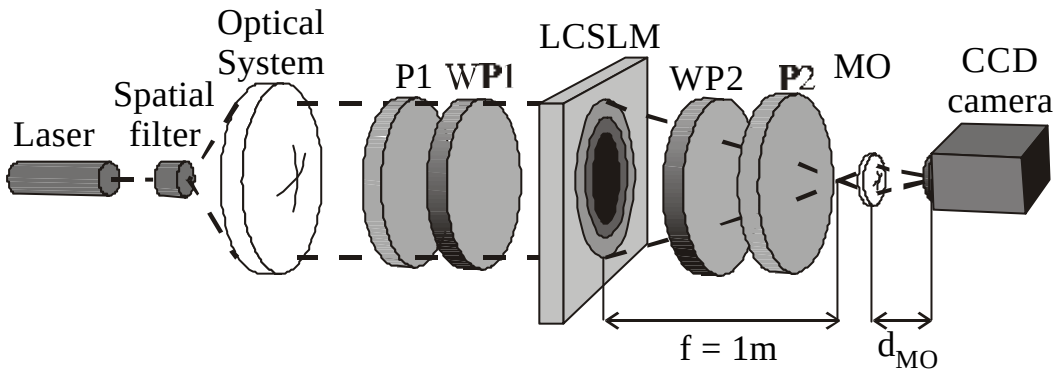


**Figure 3.15.** Scheme of the optical set-up for diffractive optics elements in the LCSLM in the phase-only regime.

In both papers [PAPER D, PAPER E] we have measured the inherent equivalent apodizing effect. In [PAPER E] we use a shorter wavelength and the lens has a larger aperture than in [PAPER D]. This makes that the inherent equivalent apodizing effect is stronger and clearer on the results presented in [PAPER E] than on the results in [PAPER D]. In this Section we reproduce the results of [PAPER E]. We use light from an Argon laser with a wavelength of 458 nm. The beam is filtered, expanded and collimated. Then it is sent through the LCSLM inserted between the polarizers and the wave plates. We need the LCSLM working in the phase-only regime. To achieve this we take advantage of the configuration that we named as the “general configuration” in Table 2.3. The phase retardance values are 125 and 95 degrees for the input (WP1) and the output (WP2) wave plates respectively. We remember that the values for the angles of the transmission axis of the input polarizer (P1) and the slow axis of the input

wave plate (WP1) is 26 deg and 0 deg respectively with respect to the director axis in the input face of the LCSLM. For the transmission axis of the output polarizer (P2) and the slow axis of the output wave plate (WP2) the angles are -16 deg and 11 deg respectively with respect to the director axis in the output face of the LCSLM. This configuration provides excellent values for phase-only performance as we discussed in Section 2.3.2. In Figure 2.30 we plotted the intensity and the phase-shift curves for this configuration and in Figure 2.31 we showed the complex amplitude transmittance in the complex plane. In order to display phase-encoded elements in the LCSLM working in the phase-only regime we have generated a calibration phase versus gray level look-up table using the phase-shift curve in Figure 2.30(b).

The spot focused by the lens encoded on the LCSLM is magnified, Figure 3.15, with a microscope objective and imaged onto a CCD camera. The microscope objective (MO) also serves as a spatial filter to eliminate higher-order diffracted images caused by the pixel structure of the SLM. To examine various defocus planes, we fix the distance $d_{MO}$ between the microscope objective and the detector and we translate the entire objective-detector system. The Fresnel lens implemented in the SLM has a focal length of 1 meter and a radius of 204 pixels, i.e. 8.4252 mm. The LCSLM we use has square pixels with a side size $W$ of 34 μm and separated by a distance $D$ of 41.3 μm.

We have obtained measurements with 12 annular masks. The central radius $r_R$ of the different masks has been designed in order to be able to sample the equivalent amplitude transmission profile along the whole aperture of the lens. In Figure 3.16 we show the equivalent amplitude distribution points $t(r_R)$ (circles) calculated from the experimental intensity measurements obtained with the 12 annular masks. The $X$-axis corresponds to the radial distance in millimeters $r'$ in the lens plane. As expected, the amplitude in the center of the focal plane decreases as the radius increases, indicative of the apodizing effect. The experimental data are fitted to a polynomial function that we show in Figure 3.16.

The polynomial function $t_P(r)$ that fits the equivalent amplitude transmission of the lens is given by

$$t_P(r) = 1 - 0.89r^2 + 0.27r^4 - 0.04r^6 \tag{3-36}$$

where we have preferred to express the polynomial function as a function of the normalized radial coordinate $r$ in the pupil plane.

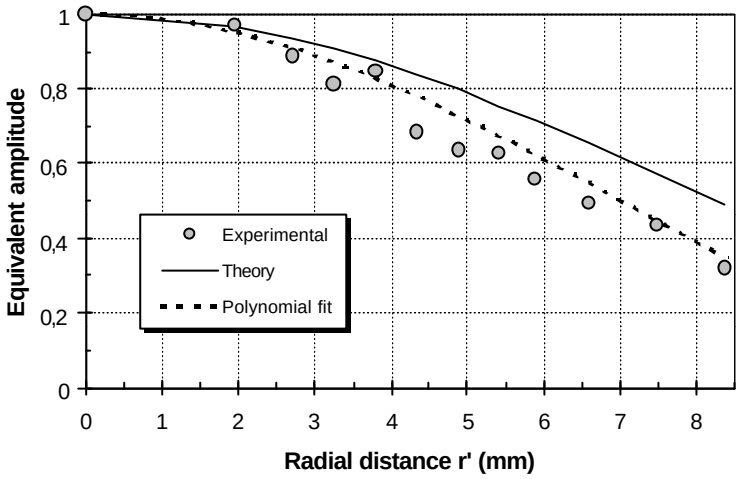


**Figure 3.16.** Amplitude distribution along the radius of the lens *r'* (in mm). The experimental data measured with the annular masks is compared with the theoretical simulation provided by the theory for the inherent equivalent apodizing effect. The experimental data are fitted with a polynomial function.

In order to compare these experimental results with the theoretically expected equivalent amplitude profile, we evaluated Eq. (3-29) with the dimensions of the pixels. The two dimensional pupil function is given by

$$t(x,y) = sinc(0.074x)sinc(0.074y) \tag{3-37}$$

where $x$ and $y$ are expressed in millimeters. The angular average $t(r)$ of this curve is numerically calculated and plotted in Figure 3.16. Actually, the angular average function $t(r)$ is practically equal to the one dimensional amplitude profile along the $X$ (or the $Y$) cartesian axis.

We note that the experimentally measured intensity is slightly lower than the theoretical values expected by the inherent apodizing effect. The difference between experiment and theory is due to the presence of aberrations in the system.

The effect of the aberrations is to send light to the sidelobes, thus producing an intensity value in the maximum lower than expected. Despite of the aberrations these measurements confirm the existence of an equivalent non-uniform transmission pupil that will produce an apodization of the point spread function (PSF) of the focused spot.

As we commented in Section 3.3, we have verified that the LCSLM we are using in this thesis does not introduce aberrations in the wave front. Nevertheless, the beam traverses a big number of optical elements (lenses, polarizers, wave plates) which in our case are responsible for the additional decrease in the equivalent amplitude profile.

### 3.5.3 Compensation method

Along the previous Section we have measured and calculated the equivalent non-uniform amplitude transmission along the lens displayed on the LCSLM. The next step is to provide some method to compensate for this amplitude profile. Normally we want to remove the apodizing effect on the response of the pixelated lens so that it can provide the same performance as a refractive lens of equal focal length and aperture. To compensate for this apodizing effect, one should use a filter with an amplitude transmission $t_I(r)$ equal to the inverse function of the equivalent amplitude profile described by the polynomial $t_P(r)$ in Eq. (3-36). The amplitude transmission of the inverse of this polynomial is displayed with the lens using the procedure developed in Section 3.4. This procedure makes possible to encode amplitude and phase information onto a LCSLM working in the phase-only regime. In this way the apodizing effect due to the pixelated structure of the LCSLM is compensated.

The inverse function $t_I(u,v)$ is calculated applying the condition $t_P(r)t_I(r)=k$ where $k$ is a constant. We are working with passive devices, i.e. they do not add energy to the wave front, therefore $t_P(r)\le 1$ and $t_I(r)\le 1$.

Then, $k \leq 1$ and in order to maximize the transmission of the inverse function $t_I(r)$ we set $k$ equal to the minimum transmission value of $t_P(r)$ in Eq. (3-36).

In Section 3.2 we showed the theoretical results expected for the axial and for the transverse response in the BIP for the clear aperture. These are the results expected if no inherent equivalent apodizing effect is present along the aperture of the lens on the LCSLM. We want to compare the numerical results when the inherent equivalent amplitude is considered and when it is not considered. In Figure 3.17 we show, respectively in *curve* ***a*** and in *curve* ***b***, the numerical axial responses due to the clear aperture and to the equivalent amplitude function described by $t_P(r)$ in Eq. (3-36). The axial responses are plotted as a function of the coordinate $W_{20}$, and the intensity values are normalized to the unit for both *curves* ***a*** and ***b***, i.e. normalization N2 explained in Section 3.2. We observe that the axial response for the function $t_P(r)$ is axially apodized, and we can clearly see that the first minimum is not zero as in the clear aperture.

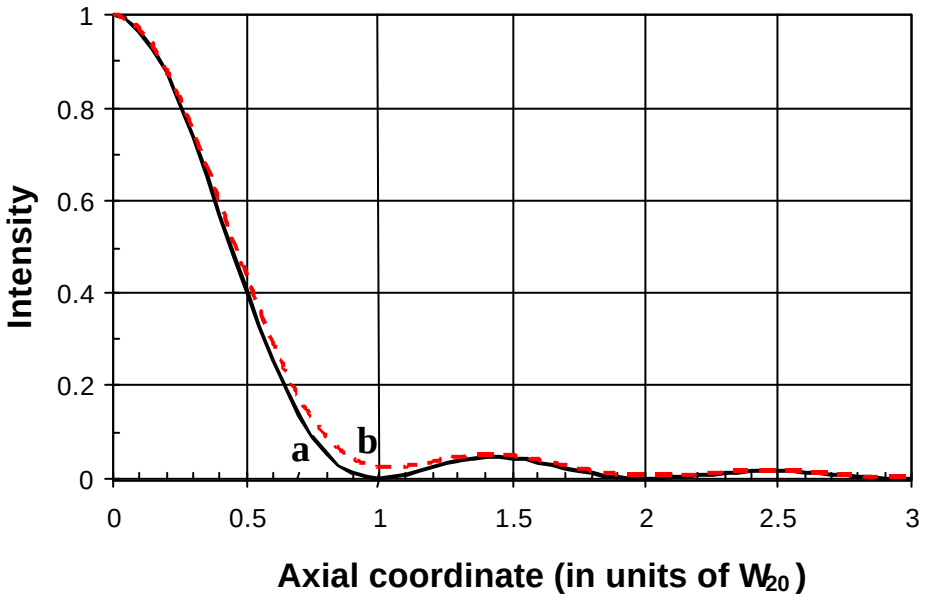


**Figure 3.17.** Numerically calculated intensity as a function of normalized axial coordinate $W_{20}$ for the amplitude pupil functions: **a**, uniform transmission; **b**, equivalent amplitude function ($t_P(r) = 1 - 0.89r^2 + 0.27r^4 - 0.04r^6$).

In Table 3.7 we have summarized the values for the positions of the axial maxima and minima for the clear aperture and for the equivalent amplitude function. We also provide the value for the intensity according to the two possible normalizations explained in Section 3.2. We can see that the equivalent amplitude function has not shifted significantly the positions of the maxima and minima with respect to the clear aperture. The main difference is that the intensity value at the minima is not null for the function $\boldsymbol{t}_P(r)$. We can also observe that the function $\boldsymbol{t}_P(r)$ diminishes the intensity in the focus to 0.41 times the value provided by the clear aperture.

| **Clear aperture** | | | | **Equiv. amplitude** | | |
|---|---|---|---|---|---|---|
| Plane | $W_{20}$ | Intensity N1 | N2 | $W_{20}$ | Intensity N1 | N2 |
| BIP | 0 | 1 | 1 | 0 | 0.41 | 1 |
| 1rst min. | 1 | 0 | 0 | 1.05 | 0.01 | 0.025 |
| 1rst max. | 1.45 | 0.047 | 0.047 | 1.45 | 0.02 | 0.053 |
| 2nd min. | 2 | 0 | 0 | 2.02 | 0.0001 | 0.0003 |

**Table 3.7.** Characteristic parameters for the theoretical axial response for the clear aperture and for the equivalent amplitude profile $t_P(r)$.

We display in Figure 3.18 the transverse responses in the BIP as a function of the normalized transverse coordinate $\boldsymbol{r}$ for the two functions: the clear aperture in *curve* ***a***, and the equivalent amplitude function in *curve* ***b***. As expected, the function $\boldsymbol{t}_P(r)$ provides a transverse apodization. We can observe that the sidelobes have been removed and the width of the central maxima is increased with respect to the clear aperture response.

In Table 3.8 we provide the values for the positions and the intensity values at the maxima and minima points in the BIP. As we can see in Figure 3.18 *curve* ***b***, the height of the sidelobe (first maximum) is approximately zero. We consider the width of the central maximum measured from the center to the first transverse minimum. The principal maximum due to $\boldsymbol{t}_P(r)$ has increased its width a 22% with respect to the clear aperture.

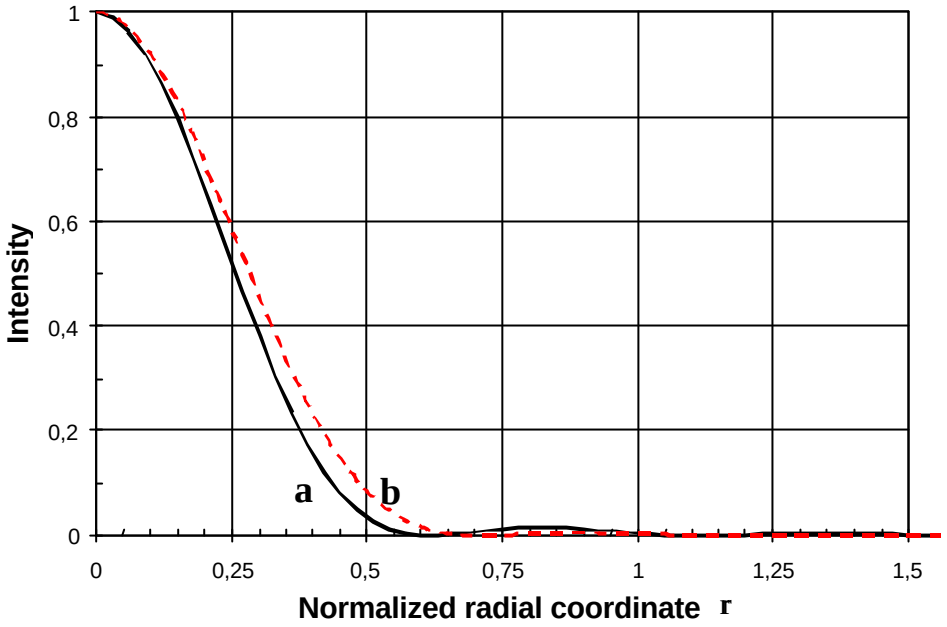


**Figure 3.18.** Theoretically calculated intensity as a function of normalized transverse coordinate $r$ in the best image plane (BIP) for the amplitude pupil functions: **a**, uniform transmission; **b**, equivalent amplitude function ($t_P(r) = 1 - 0.89r^2 + 0.27r^4 - 0.04r^6$).

| Clear aperture | | | | Equiv. amplitude | | |
|---|---|---|---|---|---|---|
| Plane | $r$ | Intensity N1 | N2 | $r$ | Intensity N1 | N2 |
| Center | 0 | 1 | 1 | 0 | 0.41 | 1 |
| 1rst min. | 0.60 | 0 | 0 | 0.73 | 3E-5 | 8E-5 |
| 1rst max. | 0.81 | 0.018 | 0.018 | 0.9 | 0.002 | 0.005 |

**Table 3.8.** Comparison between the theoretical transverse response in the best image plane (BIP) for the clear aperture and for the equivalent amplitude profile $t_P(r)$.

We have captured experimental images of the intensity distribution at some axial positions focused by the Fresnel lens displayed on the LCSLM. We use the set-up shown in Figure 3.15 and, as in Section 3.5.2, the Fresnel lens has a focal length of 1 meter and a radius of 204 pixels. We use Eq. (3-15) to calculate the numerical aperture for the optical system obtaining $NA = 0.0084$. As in Section 3.3 we deal with a low numerical aperture optical system. In order to scale the numerical normalized coordinates to the lab coordinates we calculate the axial and the transverse scale factors, given by Eq. (3-13) and Eq. (3-14), that is,

- Axial scale factor (in mm): $\frac{2\lambda(mm)}{NA^2} = 13\,mm$

- Transverse scale factor (in μm): $\frac{\lambda(mm)}{NA} = 54\,mm$

We have implemented the Fresnel lens in two different ways. On one hand, we display the quadratic phase directly on the LCSLM. This is what we label as the encoded lens. Obviously, the aperture of the encoded lens exhibits the equivalent amplitude profile $t_P(r)$ already measured. On the other hand, we encode the inverse function $t_I(r)$ onto the quadratic phase, using the procedure in Section 3.4, in order to compensate for the inherent equivalent apodizing effect. This is what we call the compensated lens. In Figure 3.19 we show the experimental images obtained with the encoded lens and with the compensated lens. These images are saturated in order to make the sidelobes visible.

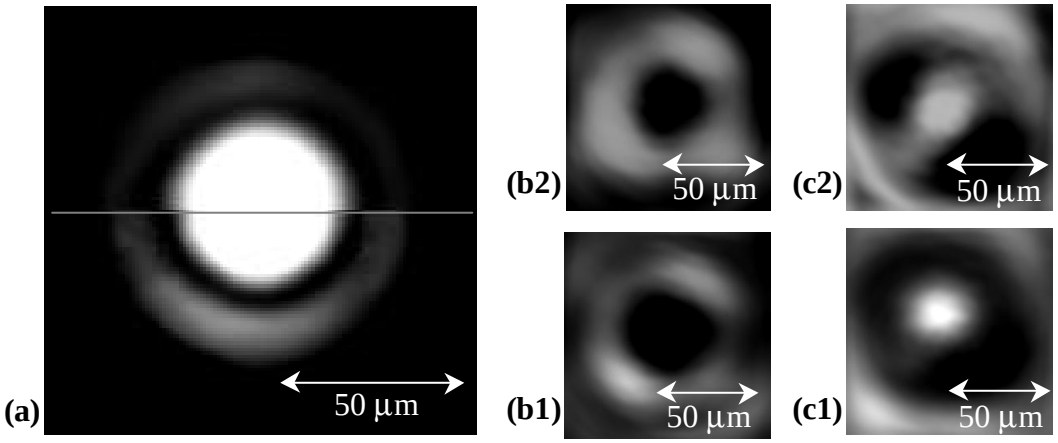


**Figure 3.19.** Experimental images of the intensity of the focused spot. (a) Combination of saturated images in the BIP (upper half, encoded lens; lower half, compensated lens). (b) and (c) are the first axial minimum and the first secondary axial maximum planes respectively. Upper row, (b1) and (c1), for the encoded lens, and lower row, (b2) and (c2), for the compensated lens.

The BIP is shown in Figure 3.19(a), where we have combined the focused spot from the encoded lens (upper half) and the compensated lens (lower half). We can see in the encoded lens (upper half) the shift in the position of the first transverse minimum and the lower intensity of the first secondary maximum. These features indicate the existence of an apodizing effect on the transverse

response of an encoded lens in the LCSLM. We provide on the figure the actual lab scale in microns for the distances in the image.

The images in Figure 3.19(b) and Figure 3.19(c) show respectively the first axial minimum and the first secondary maximum for the encoded lens (upper row) and for the compensated lens (lower row). These planes are located at the axial distances predicted numerically.

We note that the images in Figure 3.19 are not totally symmetric probably due to the existence of aberrations produced by the different elements in the set-up (polarizers, wave plates, lenses) as we commented in Section 3.5.2. Actually, the modulator that we are using is almost free of aberrations and allows us to obtain diffraction-limited images.

In Table 3.9 we compare the numerically predicted and the experimentally measured values for the intensity at the different axial positions shown in Figure 3.19. On one hand, the numerical results for the clear aperture have to be compared with the experimental results obtained with the compensated lens. On the other hand, the numerical results for the equivalent amplitude function $t_P(r)$ have to be compared with the experimental results using the directly encoded lens. There is a good agreement between the numerical and the experimental intensity values in the two cases. We remark that we have obtained the expected non-null value at the first axial minimum for the encoded lens.

| **Clear aperture (compensated lens)** | | | | **Equiv. amplit. (encoded lens)** | |
|---|---|---|---|---|---|
| Plane | *z (mm)* | Intensity N2 (theory) | Intensity N2 (exper.) | Intensity N2 (theory) | Intensity N2 (exper.) |
| BIP | 0 | 1 | 1 | 1 | 1 |
| 1$^{rst}$ min. | 13 | 0 | 0 | 0.03 | 0.03 |
| 1$^{rst}$ max. | 19 | 0.05 | 0.09 | 0.05 | 0.09 |

**Table 3.9.** Comparison between the numerical and the experimental results for the intensity values at the characteristic axial planes for the clear aperture and for the equivalent amplitude pupil function $t_P(r)$.

We show in Table 3.10 the numerical and the experimental results for the transverse response at the BIP for the clear aperture (compensated lens). In Table

3.11 these results are summarised for the equivalent amplitude function $t_P(r)$ (directly encoded lens). The experimental distance $r'$ for the radial positions in these tables is obtained as the average of a number of measurements taken at different angular positions in the image of the BIP. A reasonable estimation of the error in the determination of the radial positions is about $\pm 2$ μm. We could not measure the position for the first transverse maximum for the encoded lens, Table 3.11, because the intensity level is very close to the background.

In Table 3.10 and in Table 3.11 we can see the very good agreement between the numerical and the experimental values. The predicted positions coincide very well with the experimental measurements. It is especially interesting to note that the first minimum for the compensated lens is at the position predicted for a clear aperture pupil. This fact confirms that using the compensation procedure proposed in [PAPER D], that we have explained in this Section, we are able to compensate for the inherent equivalent apodizing effect exhibited by the pixelated lens.

| **Clear aperture (compensated lens)** | | | | |
|---|---|---|---|---|
| Position | $r'$ (mm) (theory) | Intensity N2 (theory) | $r'$ (mm) (exper.) | Intensity N2 (exper.) |
| Center | 0 | 1 | 0 | 1 |
| 1rst min. | 32.6 | 0 | 33.2 | 0 |
| 1rst max. | 44.0 | 0.02 | 41.2 | 0.03 |

**Table 3.10.** Comparison between the numerical and the experimental results for the intensity values at the characteristic transverse positions at the BIP for the clear aperture.

| **Equivalent amplitude (encoded lens)** | | | | |
|---|---|---|---|---|
| Position | $r'$ (mm) (theory) | Intensity N2 (theory) | $r'$ (mm) (exper.) | Intensity N2 (exper.) |
| Center | 0 | 1 | 0 | 1 |
| 1rst min. | 39.4 | 8E-5 | 39.9 | 0 |
| 1rst max. | 48.9 | 0.005 | --- | --- |

**Table 3.11.** Comparison between the numerical and the experimental results for the intensity values at the characteristic transverse positions at the BIP for the equivalent amplitude pupil function $t_P(r)$.

## 3.6 Focusing apodizers onto a LCSLM in phase-only regime

We commented in the first paragraph of Section 3.4 that a very powerful and attractive property of diffractive optics elements (DOEs) is the possibility to combine different functions in the same DOE. Our goal is to combine the PSF transformation property of non-uniform transmission filters with the focusing property of lenses. This new device is what we called in Section 3.4 the programmable focusing apodizer, whose focal length and action on the PSF of the system can both be changed in real time. To generate this combined element on the LCSLM we have to overcome two limitations that have been the focus of Section 3.4 and Section 3.5. In a recent paper [PAPER E] we demonstrated experimentally that we are able to combine non-uniform amplitude transmission filters together with a Fresnel lens onto the LCSLM working in the phase-only regime. In this Section we will introduce and complement these results.

We have selected three filters with very different features in the BIP and along the axis. We want to show the wide range of programmable focusing apodizers that can be implemented using the technique we propose. These three amplitude filters were introduced in Section 3.2. They are the axial hyperresolving, the transversal apodizing and the transversal hyperresolving filters, whose profiles we showed in Figure 3.2 as a function of the normalized radial coordinate $r$ in the pupil plane.

We note that the transmission in the pupil is modified by the inherent equivalent apodizing effect, treated in Section 3.5. In this Section the Fresnel lens that we implement has the same values as in previous Section 3.5.2 and Section 3.5.3, i.e. 1 meter of focal length and 204 pixels of radius. We note that the experimental set-up to produce the programmable focusing apodizers is the one we showed in Figure 3.15. Therefore, the results presented in Section 3.5.2 for the equivalent amplitude profile across the aperture of the lens remain valid and they are described by the function $t_P(r)$ in Eq. (3-36). The equivalent amplitude function $t_P(r)$ modifies the amplitude profile of any amplitude filter that is

encoded with the lens onto the LCSLM. The resultant amplitude transmission on the exit pupil for the programmable focusing apodizers is given by the product of the desired amplitude filter and the function $t_P(r)$. In Figure 3.20 we show the modified amplitude profile on the exit pupil for the three filters.

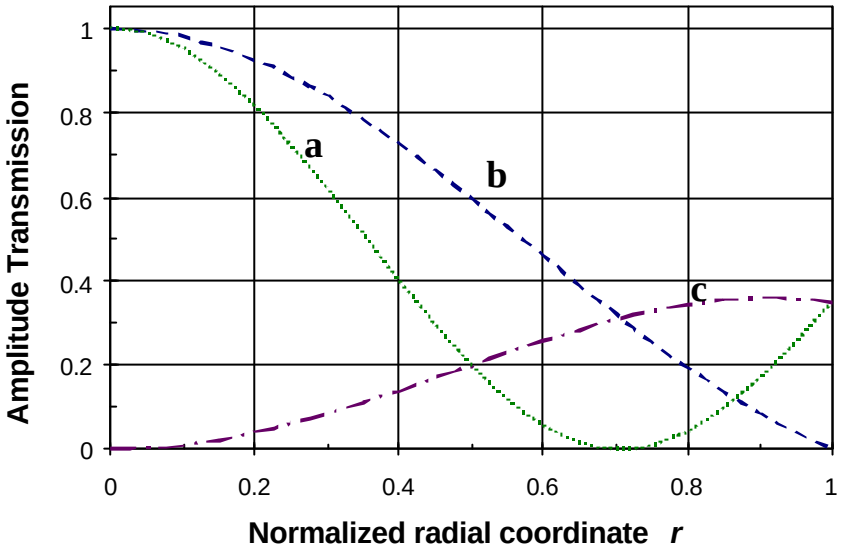


**Figure 3.20.** Amplitude pupil filter functions modified by the equivalent amplitude function function $t_P(r) = 1 - 0.89r^2 + 0.27r^4 - 0.04r^6$. **a**, axial hyperresolving filter ($t(r) = (1 - 4r^2 + 4r^2) * t_P(r)$); **b**, transverse apodizing filter ($t(r) = (1 - r^2) * t_P(r)$); **c**, transverse hyperresolving filter ($t(r) = r^2 * t_P(r)$).

Thus, we intend to produce the filters described in Figure 3.2, but due to the inherent equivalent apodizing effect, we obtain the filters shown in Figure 3.20. Note that the transmission of the transversal apodizing filter is practically equal in both figures, while the profile for the transversal hyperresolving filter is greatly distorted with respect to the desired case. The axial multifocusing filter is also distorted. Therefore, to obtain the desired amplitude transmission on the exit pupil we have to compensate for the equivalent amplitude function $t_P(r)$, as we did in Section 3.5.3. For each filter, we multiply the corresponding amplitude profile by the function $t_I(r)$, which is the inverse of $t_P(r)$. The resultant amplitude profile is a compensated version of the filter where the inherent equivalent apodizing effect has been removed. To implement the combination of

an amplitude filter and the Fresnel lens onto the LCSLM working in the phase-only regime we use the encoding procedure developed in Section 3.4.

We want to show the distortion produced by the inherent equivalent apodizing effect, given by the function $t_P(r)$, on the response for the programmable focusing apodizers. When this distortion is important, the compensation for the inherent apodizing effect is totally justified. To show this we provide the results obtained for the transverse apodizing and for the transverse hyperresolving filters in the BIP.

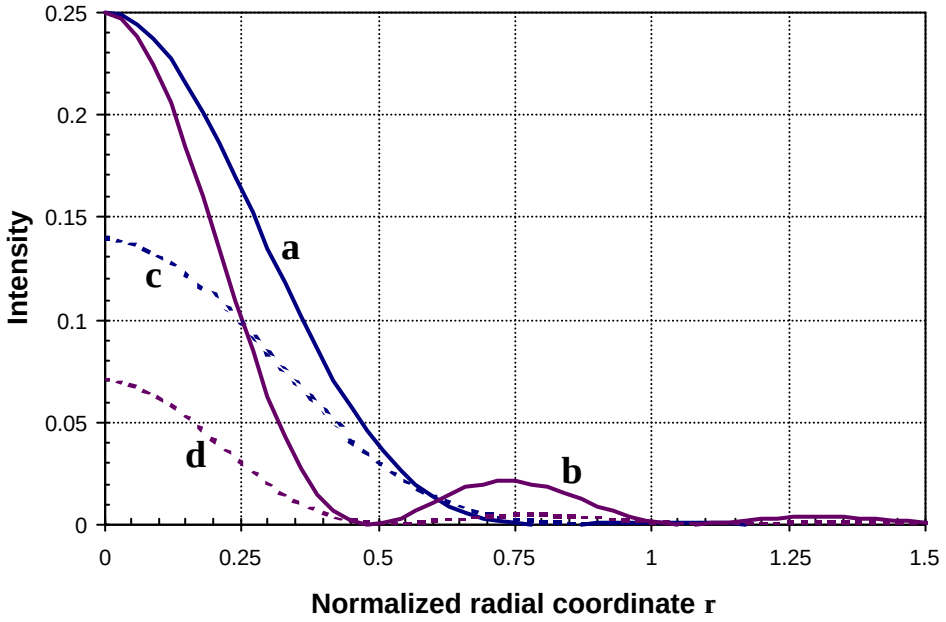


**Figure 3.21.** Theoretically calculated intensity as a function of normalized transverse coordinate $r$ in the best image plane (BIP) for the amplitude pupil functions: **a**, transverse apodizing filter ($t(r) = 1 - r^2$); **b**, transverse hyperresolving filter ($t(r) = r^2$); **c**, modified transverse apodizing filter ($t(r) = (1 - r^2) * t_P(r)$); **d**, modified transverse hyperresolving filter ($t(r) = r^2 * t_P(r)$).

In Figure 3.21 we show the numerically calculated transverse responses in the BIP as a function of the normalized radial coordinate $r$. *Curves* ***a*** and ***c*** are the responses for the transverse apodizing filter when there is no inherent apodizing effect in the pupil and when this effect, described by $t_P(r)$, exists. Similarly, *curves* ***b*** and ***d*** are the responses for the transverse hyperresolving filter when there is no inherent apodizing effect in the pupil and when this effect, described

by $t_P(r)$, exists. Actually, *curves* ***a*** and ***b*** have been previously reported in Figure 3.5 as *curves* ***d*** and ***e*** respectively. The intensity values are normalized to the peak value corresponding to the clear aperture, i.e. normalization N1. The most evident point to remark is that when no inherent apodizing effect exists, *curves* ***a*** and ***b***, the peak intensities are equal for both filters. When the inherent equivalent apodizing effect described by $t_P(r)$ is present, the filter $(1-r^2)$ gives a peak that is twice more intense than the maximum given by the filter $r^2$.

| $t(r) = 1 - r^2$ | | | | $t(r) = (1 - r^2) * t_P(r)$ | | |
|---|---|---|---|---|---|---|
| Plane | $r$ | Intensity N1 | N2 | $r$ | Intensity N1 | N2 |
| Center | 0 | 0.25 | 1 | 0 | 0.14 | 1 |
| 1rst min. | 0.81 | 0 | 0 | 0.95 | 3E-7 | 2E-6 |
| 1rst max. | 1.02 | 0.001 | 0.004 | 1.13 | 1E-4 | 8E-4 |

**Table 3.12.** Comparison between the theoretical transverse response in the best image plane (BIP) for the transverse apodizing filter and for the transverse apodizing filter modified by the equivalent amplitude function $t_P(r)$.

| $t(r) = r^2$ | | | | $t(r) = r^2 * t_P(r)$ | | |
|---|---|---|---|---|---|---|
| Plane | $r$ | Intensity N1 | N2 | $r$ | Intensity N1 | N2 |
| Center | 0 | 0.25 | 1 | 0 | 0.07 | 1 |
| 1rst min. | 0.48 | 5E-5 | 2E-4 | 0.53 | 1E-5 | 2E-4 |
| 1rst max. | 0.72 | 0.02 | 0.09 | 0.78 | 0.005 | 0.07 |

**Table 3.13.** Comparison between the theoretical transverse response in the best image plane (BIP) for the transverse hyperresolving filter and for the transverse hyperresolving filter modified by the equivalent amplitude function $t_P(r)$.

In Table 3.12 and in Table 3.13 we provide further details for the theoretical response for the filters shown in Figure 3.21. In Table 3.12 we analyse the transverse apodizing filter, and in Table 3.13 the results for the transverse hyperresolving filter are given. In Table 3.12 we observe the apodization of the response when there is inherent equivalent apodizing effect on the pupil: the width of the principal maximum is increased to a value of $r$=0.95, and the height of the first sidelobe has decreased in one order of magnitude. The distortion caused by the inherent equivalent apodizing effect can also be observed in Table 3.13: the

width of the main maximum is increased by 10%. This width is measured from the center to the first transverse minimum.

In Figure 3.22 we show the experimental images obtained when we directly send the programmable focusing apodizers to the LCSLM and do not compensate for the inherent apodizing effect. Figure 3.22(a) corresponds to the transverse apodizing filter while Figure 3.22(b) corresponds to the transverse hyperresolving filter. In the experimentally obtained images we can still see the apodizing and hyperresolving effects. The central maximum is wider for the apodizing filter than for the hyperresolving filter. Nevertheless, the inherent equivalent apodizing effect is adding some apodization to the PSF of both filters. Measurements carried out on these experimental images show that as predicted the intensity distribution is distorted by the inherent equivalent apodizing effect, described by the function $\boldsymbol{t}_P(r)$. The most significant result in this direction is the relation between the peak intensities measured on the two images. The experimental intensity values in the maxima for the apodizing and the hyperresolving filters are 190 and 95 respectively as we show in Figure 3.22. These intensity values are measured in gray levels of the frame grabber. The ratio between them is about 0.5, which coincides with the numerical ratio between the maxima for the *curves* **c** and **d** in Figure 3.21, corresponding respectively to the transverse apodizing and the transverse hyperresolving filters modified by $\boldsymbol{t}_P(r)$.

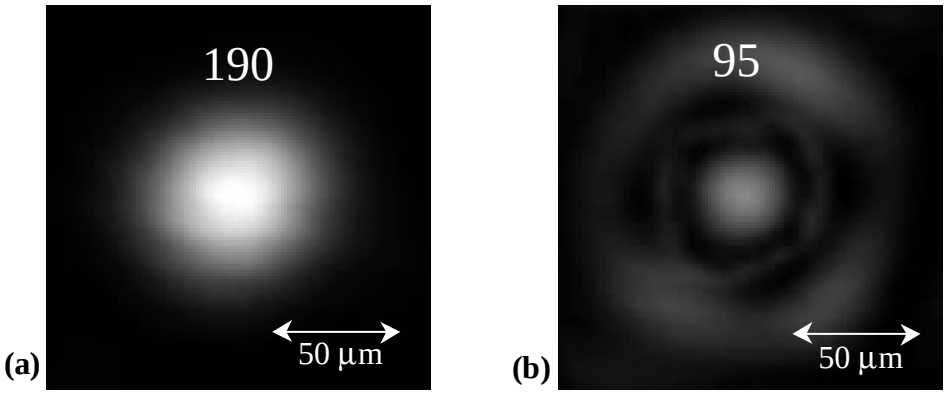


**Figure 3.22.** Experimental images of the intensity of the focused spot when the inherent apodizing effect is not compensated. (a) transversal apodizing filter; (b) transversal hyperresolving filter.

We have performed distance and intensity measurements of the characteristic points on the two images in Figure 3.22. In Table 3.14 for the apodizing filter and in Table 3.15 for the hyperresolving filter, we compare the experimental measurements with the numerically predicted values. The distance measurements are expressed in microns. The predicted values $r'$ in microns are calculated by scaling the normalized $r$ values given in Tables 3.12 and 3.13 to the lab coordinates. In both tables, Tables 3.14 and 3.15, there is a very good agreement between the experimental and the numerical results. We remark the excellent accordance between the experimental and the predicted radial positions. This accordance confirms the shift in the positions of the first minimum and the first secondary maximum due to the inherent equivalent apodizing effect. The first secondary maximum for the transverse apodizing filter, Table 3.14, can not be measured because it has a very low intensity value close to the background.

| $t(r) = (1 - r^2)$ (no compensation) | | | | |
|---|---|---|---|---|
| Position | $r'$ (mm) (theory) | Intensity N2 (theory) | $r'$ (mm) (exper.) | Intensity N2 (exper.) |
| Center | 0 | 1 | 0 | 1 |
| 1rst min. | 51.6 | 2E-6 | 52.3 | 0 |
| 1rst max. | 61.1 | 8E-4 | --- | --- |

**Table 3.14.** Comparison between the numerical and the experimental results for the intensity values at the characteristic positions at the BIP for the transverse apodizing filter (no compensation).

| $t(r) = r^2$ (no compensation) | | | | |
|---|---|---|---|---|
| Position | $r'$ (mm) (theory) | Intensity N2 (theory) | $r'$ (mm) (exper.) | Intensity N2 (exper.) |
| Center | 0 | 1 | 0 | 1 |
| 1rst min. | 28.5 | 2E-4 | 28.8 | 0 |
| 1rst max. | 42.1 | 0.07 | 40.8 | 0.09 |

**Table 3.15.** Comparison between the numerical and the experimental results for the intensity values at the characteristic positions at the BIP for the transverse hyperresolving filter (no compensation).

We have verified experimentally that the response for the two amplitude filters is distorted because of the inherent apodizing effect. Now, we introduce in the programmable focusing apodizers the compensation given by the inverse function $t_I(r)$. These compensated programmable focusing apodizers produce

the experimental intensity distribution in the BIP that we show in Figure 3.23. Figure 3.23 (a) corresponds to the transverse apodizing filter while Figure 3.23 (b) corresponds to the transverse hyperresolving filter. We can easily visualize the apodizing and hyperresolving effects produced by these filters in the BIP.

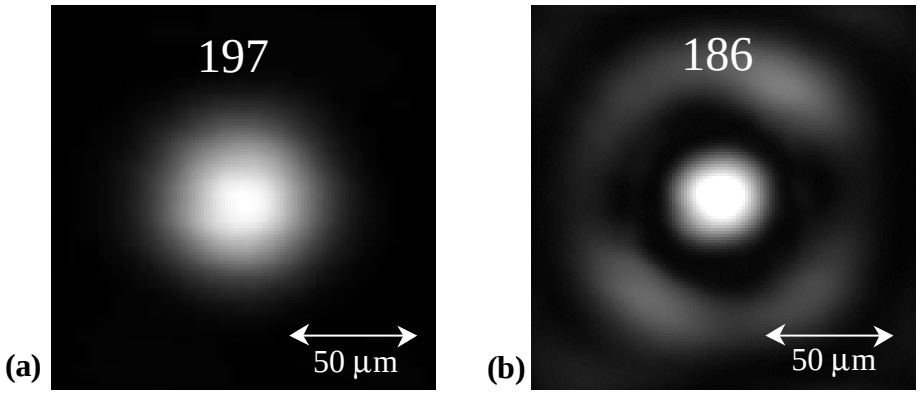


**Figure 3.23.** Experimental images of the intensity of the focused spot when the inherent apodizing effect has been compensated. (a) transversal apodizing filter; (b) transversal hyperresolving filter.

| $t(r) = 1 - r^2$ *(compensated)* | | | | |
|---|---|---|---|---|
| Position | *r' (mm)* (theory) | Intensity N2 (theory) | *r' (mm)* (exper.) | Intensity N2 (exper.) |
| Center | 0 | 1 | 0 | 1 |
| 1rst min. | 44.0 | 0 | 49.6 | 0 |
| 1rst max. | 55.4 | 0.004 | --- | --- |

**Table 3.16.** Comparison between the numerical and the experimental results for the intensity values at the characteristic positions at the BIP for the transverse apodizing filter (compensated).

| $t(r) = r^2$ *(compensated)* | | | | |
|---|---|---|---|---|
| Position | *r' (mm)* (theory) | Intensity N2 (theory) | *r' (mm)* (exper.) | Intensity N2 (exper.) |
| Center | 0 | 1 | 0 | 1 |
| 1rst min. | 26.1 | 2E-4 | 27.9 | 0 |
| 1rst max. | 39.1 | 0.09 | 39.4 | 0.11 |

**Table 3.17.** Comparison between the numerical and the experimental results for the intensity values at the characteristic positions at the BIP for the transverse hyperresolving filter (compensated).

Our goal is to verify that we have removed the distortion caused by the inherent apodizing effect. The peak values of intensity measured in Figure 3.23(a) and (b) are 197 and 186 respectively. Therefore, they are practically equal and this

result is in a clearly good agreement with the predicted results for the case when no inherent apodizing effect exists.

In Tables 3.16 and 3.17 we compare experimental measurements carried out on the images in Figure 3.23 with the numerically predicted values provided in Tables 3.12 and 3.13. In both tables, Tables 3.16 and 3.17, we find a very good agreement between the experimental and the predicted values. It is especially important the confirmation that the radial maxima and minima occur at the predicted positions. Therefore, we have verified that when the inherent apodizing effect is compensated the desired optical response is recovered.

Finally, we demonstrate that we are able to generate the axial hyperresolving filter encoded onto the Fresnel lens. We compensate for the inherent apodizing effect in order to generate the numerically predicted axial response shown in Figure 3.4 curve (c), in which we can see the characteristic multifoci behavior of this filter: it produces very high secondary maxima along the axis.

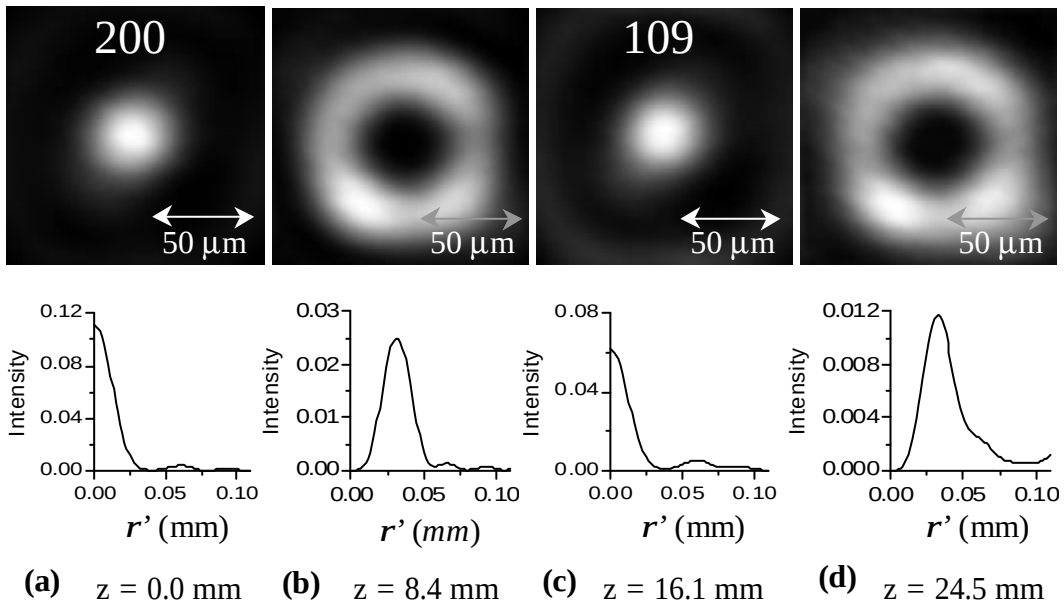


**Figure 3.24.** Experimental images of the intensity at various defocus planes for the axial hyperresolving filter compensated for the inherent equivalent apodizing effect. In the first row the experimental images are shown, in the second row the corresponding numerically calculated transverse responses.

In Figure 3.24 we show the experimental images captured at different defocused planes. These images have been digitally saturated to show the sidelobes in the transverse response. The numerically calculated transverse responses at these planes are shown in the second row. The intensity values in the numerical graphs are normalized with respect to the peak value for the clear aperture (normalization N1). The *X*-axis in the numerical graphs is scaled to the radial lab coordinate $r'$ in millimeters. The origin of coordinates ($r' = 0$ mm) corresponds to the center of the experimental images in the first row. The planes (a) and (c) show the principal maximum and the first secondary maximum, and the planes (b) and (d) show the first and the second axial minimum. These planes coincide with the axial position predicted numerically, that is indicated in millimeters underneath each figure.

In Figure 3.24(b) and Figure 3.24(d), which correspond to the positions of the minima along the axis, the transverse responses present a ring. The positions for these rings, that can be determined using the length scale on the figure, agree very well with the numerical prediction (second row). In Figure 3.24(a) and Figure 3.24(c), we show the values of the gray levels for the peak intensity for the best image plane (200) and for the first secondary maximum (109). The experimental ratio of the intensity of the first secondary maxima with respect to the peak intensity in the best image plane is 0.55, which agrees with the theoretical ratio (0.56) given in Table 3.1. We can also observe this ratio looking at the intensity values for the numerically calculated figures in the second row in Figure 3.24.

Along this Section we have demonstrated the feasibility of combining different functions in the same DOE. We have generated programmable focusing apodizers which can modify the PSF and the focal length in real time. We have verified that the agreement between the experiment and the numerical predictions is excellent.

# 4 CONCLUSIONS

In the first part of this thesis we have presented a new reverse-engineering approach which provides accurate prediction of the optical transmission of the TN-LCSLM. In the second part we have demonstrated the possibility of generating programmable apodizers and programmable focusing apodizers with the requested performance. Among the several results provided along the thesis we emphasize the following:

- We have developed a simplified model to describe the molecular director orientation $\vec{n}$ across the TN-LCSLM. The model includes the molecules near either edge of the LCSLM that are unable to twist and tilt under an applied voltage. This edge effect depends on the magnitude of the applied voltage. We have calculated an analytical expression for the Jones matrix of the TN-LCSLM according to the proposed model.

- We have characterized the voltage independent parameters of the TN-LCSLM by means of a reverse-engineering approach.

- We have demonstrated a technique to experimentally measure the birefringences of both the central part and the edge layers of the TN-LCSLM as a function of the applied voltage (gray scale levels).

- The proposed reverse-engineering approach confirms that in the field-off state there is no edge effect. Nevertheless, we have confirmed that in the field-on state the edge effect is very significant: the ratio between the maximum birefringences for the edge layers and the central part, $2\delta_{max}/\beta_{max}$, tell us that the edge layers can represent a 22% of the total thickness of the LCSLM.

- We have demonstrated the capability of the approach to predict with a high degree of accuracy the amplitude and phase modulations as a function of the applied voltage (gray scale level). We have shown that the new approach improves significantly the accuracy with respect to previous reverse-engineering approaches.

- Using the new approach, we have proved that we can perform computer searchs to calculate the optimum configuration of the polarizing elements in front of and behind the TN-LCSLM leading to a desired modulation behavior of the set-up. We have looked for polarization configurations leading to phase-only modulation or amplitude-only modulation, which are interesting configurations in a number of applications.

- A generalised architecture to generate and detect elliptically polarized light has been proposed. It has been shown that adding wave plates to the optical set-up (in front of and behind the TN-LCSLM) greatly improves the modulation capabilities of the TN-LCSLM. We have also shown that the concept of the average eigenvector to obtain phase-only modulation is a particular case of the more general approach to generate and detect elliptically polarized light that we have presented.

- We have proved that we can obtain amplitude-only and phase-only modulations with thin LCDs by adding wave plates to the optical system and by lowering the wavelength of the incident light.

- We have analysed theoretically several possible actions that a non-uniform transmission filter may perform on the PSF of an optical system: axial apodization, axial hyperresolution, transverse apodization at the BIP, and transverse hyperresolution at the BIP. The PSF for the clear aperture has also been calculated, serving as a reference to classify the action of the different filters.

- We report the use of TN-LCSLMs, in the amplitude-only regime, to display non-uniform transmission filters, the so-called programmable apodizers. We have displayed an axially apodizing filter, an axially hyperresolving filter, a transverse apodizing filter, a transverse hyperresolving filter, and the uniform transmission filter (clear aperture).

- The measurements done on the point-spread function (PSF) of the optical system confirm the optimum performance of the programmable apodizers. By means of the technique we propose it is very easy to implement any amplitude filter. Moreover, the technique permits the rapid modification of the PSF of an optical system.

- We have developed a method to encode complex amplitude information onto a quadratic phase-encoded function. This method is both valid for high and for low resolution media. We have used it to encode the amplitude filters onto the Fresnel lens, and we call this new device programmable focusing apodizer.

- We have shown both theoretically and experimentally an apodizing effect which is inherent to the encoding of a lens, or any other focusing element, in a pixelated device, such as the TN-LCSLM. We have called this phenomenon the inherent equivalent apodizing effect. This effect apodizes the PSF of an optical system. We have obtained the same result both using an image formation approach and a diffraction efficiency approach.

- From the diffraction efficiency approach, the equivalent non-uniform amplitude profile across the exit pupil can be viewed as originated by the local change in the diffraction efficiency across the aperture of the lens. This change

in the diffraction efficiency is produced by the variation in the number of pixels per period.

- We have proposed a method to measure and compensate for the inherent equivalent apodizing effect. A non-uniform transmission filter that compensates for the equivalent non-uniform transmission profile across the exit pupil is encoded onto the lens. Experimental results have proved that the inherent equivalent apodizing effect can be removed.

- We have demonstrated that a phase-only TN-LCSLM can be used to generate the programmable focusing apodizer, i.e. the combination of a lens and a non-uniform amplitude transmission filter in a single DOE. We have implemented an axially hyperresolving filter, a transverse apodizing filter, a transverse hyperresolving filter, and the uniform transmission filter (clear aperture).

- Experimental measurements of the PSF for the different programmable focusing apodizers are in excellent agreement with the numerical predictions. The technique permits the rapid modification of the PSF and/or the focal length of an optical system.

# APPENDIX: PIXELATED PHASE-BLAZED GRATING AND THE INHERENT EQUIVALENT APODIZING EFFECT

In Section 3.5.1 we developed the theory for the inherent equivalent apodizing effect based on the approach by Carcolé *et al.* We obtained Eq. (3-29), which describes the equivalent amplitude profile along the aperture of a lens displayed on a pixelated device, such as the LCSLM. In this Appendix we show an alternative theoretical approach to study the inherent equivalent apodizing effect. This theoretical approach deals with the concept of diffraction efficiency. The diffraction efficiency is the fraction of the incident light that is distributed into a certain diffraction order. This approach is not as general as the one given in Section 3.5.1, however, it provides an intuitive explanation of the phenomenon of the inherent equivalent apodizing effect.

We give the outline of this Appendix. First, we will develop the expressions for the diffraction efficiency of a phase-blazed grating displayed on a pixelated device. Then, we will see that a Fresnel lens can be considered as a phase blazed grating with a spatially variable period. This fact enables us to obtain

the expression for the local diffraction efficiency exhibited by the Fresnel lens along its aperture. Actually, this local diffraction efficiency expression coincides with the equivalent amplitude profile, Eq. (3-28), in Section 3.5.1. Through all the Appendix we consider a one dimensional geometry. Finally, we will generalise the results to the case of the two dimensional geometry.

In a LCSLM, not the whole pixel area is transmissive. A part of the pixel, the dead area occupied by the electrode wires, is blocking the pass of light as we showed in Figure 3.12. We have to take into account this dead area into the theoretical development that follows. Our goal is to calculate the analytical expressions for the diffraction efficiency of a phase-blazed grating displayed on the LCSLM.

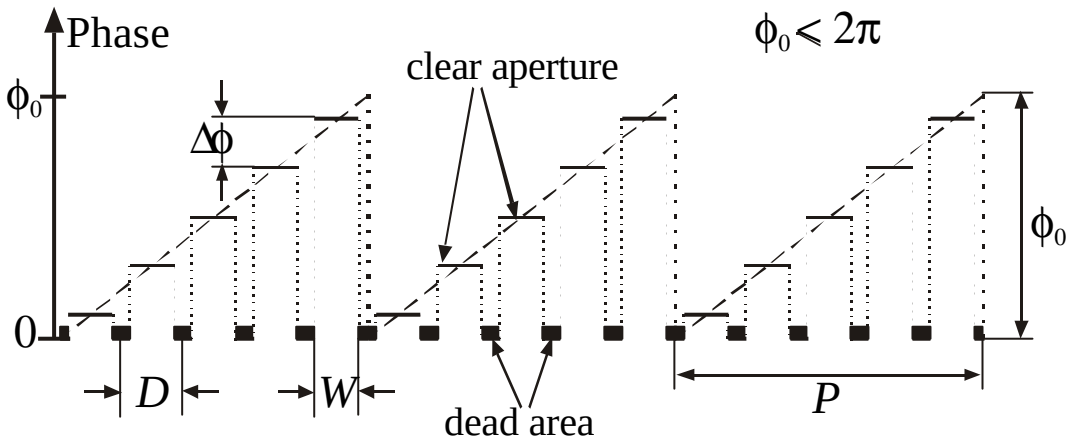


**Figure A.1.** Phase profile for a multilevel blazed grating displayed on a pixelated device. In certain pixelated devices, as the LCSLMs, we note the existence of dead areas that do not transmit the light.

In Figure A.1 we show the phase profile for a blazed grating with period $P$, phase depth $f_0$, defined along a length $L$. We limit the phase depth $f_0$ to a maximum value of $2\pi$ radians. This simplification does not represent any loss of generality because equal phase values (modulus $2\pi$) produce the same effect. Note in Figure A.1 the existence of dead areas in the pixels. Consequently, we distinguish between the distance between pixels $D$ and the width $W$ of the clear aperture of the pixel. The pixelated structure of the LCSLM samples the blazed profile with a sampling period $D$. The sampling generates a quantization of the

phase profile, with $Df$ being the value for the phase jump between consecutive pixels. It is important to note, as we represent in Figure A.1, that along the clear aperture width *W* of the pixel the phase is a constant, thus, the blazed grating has a stepped phase profile. First, we calculate the analytical expression for the phase profile illustrated in Figure A.1. Then, the diffraction efficiencies for the different diffracted orders will be obtained as the Fourier transform of this analytical expression.

Let us calculate the analytical expression for the phase profile. According to the notation in Figure A.1, the phase-blazed profile has a slope $f_0/P$, repeated with a periodicity $P$, i.e.,

$$\left[\exp\left(i\frac{f_0}{P}x\right)rect\left(\frac{x}{P}\right)\right]\otimes\sum_{n=-\infty}^{+\infty}d(x-nP) \qquad \text{(A-1)}$$

with the usual definitions for the rectangle and for the delta functions [Goo96]. The complex exponential in expression (A-1) represents a linear phase with a slope $f_0/P$. This linear phase profile is limited to a period $P$ by the *rectangle* function, and it is periodically repeated with a periodicity P by the array of delta functions.

Now, the blazed grating in expression (A-1) needs to be sampled with a sampling period *D*, equal to the separation between the pixels. The sampled points are then convolved by the clear aperture $W$ of the pixel to obtain the stepped profile shown in Figure A.1. This convolution leads to a constant phase value along the width *W* for the clear aperture of the pixels. Thus, the expression for the amplitude transmission $t(x)$ (we use coherent illumination) for the blazed grating is

$$t(x)=\left\{\left\{\left[\left[\exp\left(i\frac{f_0}{P}x\right)rect\left(\frac{x}{P}\right)\right]\otimes\sum_{n=-\infty}^{+\infty}d(x-nP)\right]\sum_{k=-\infty}^{+\infty}d(x-kD)\right\}\otimes rect\left(\frac{x}{W}\right)\right\}rect\left(\frac{x}{L}\right) \qquad \text{(A-2)}$$

where we have taken into account the finite extent $L$ for the grating. Using the definition for the *comb* function

$$comb\left(\frac{x}{D}\right)=\sum_{k=-\infty}^{+\infty}\delta(x-kD) \tag{A-3}$$

we can express Eq. (A-2) in a more compact form, i.e.,

$$t(x)=\left\{\left\{\left[\left[\exp\left(i\frac{f_0}{P}x\right)rect\left(\frac{x}{P}\right)\right]\otimes comb\left(\frac{x}{P}\right)\right]comb\left(\frac{x}{D}\right)\right\}\otimes rect\left(\frac{x}{W}\right)\right\}rect\left(\frac{x}{L}\right) \tag{A-4}$$

We Fourier transform Eq. (A-4) where we apply the next typical pairs of transforms,

$$comb\left(\frac{x}{P}\right)\leftrightarrow P\,comb(Pu) \tag{A-5a}$$

$$rect\left(\frac{x}{P}\right)\leftrightarrow P\,\mathrm{sinc}(Pu) \tag{A-5b}$$

$$\exp\left(i\frac{f_0}{P}x\right)\leftrightarrow\delta\left(u-\frac{f_0}{2\pi P}\right) \tag{A-5b}$$

We also take into account the convolution theorem. As a result the amplitude distribution $T(u)$ in the Fourier plane is given by

$$T(u)=\left\{\left\{\left[\left(\delta\left(u-\frac{f_0}{2\pi P}\right)\otimes P\,sinc(Pu)\right)P\,comb(Pu)\right]\otimes D\,comb(Du)\right\}W\,sinc(Wu)\right\}\otimes L\,sinc(Lu) \tag{A-6}$$

We proceed with the first convolution,

$$\delta\left(u-\frac{f_0}{2\pi P}\right)\otimes Psinc(Pu)=Psinc\left[P\left(u-\frac{f_0}{2\pi P}\right)\right] \tag{A-7}$$

We see that the shift in the *sinc* function is linearly related with the slope $f_0/P$ for the blazed profile. Using Eq. (A-7) and the explicit expression for the functions *comb(Pu)* and *comb(Du)* we rewrite Eq. (A-6) as follows,

$$T(u)=\left\{\left\{\left[\left[ P\,sinc\left[P\left(u-\frac{f_0}{2pP}\right)\right]P\sum_{n=-\infty}^{+\infty} d\left(u-n\frac{1}{P}\right)\right]\otimes D\sum_{k=-\infty}^{+\infty} d\left(u-k\frac{1}{D}\right)\right]W\ sinc(Wu)\right\}\otimes L\ sinc(Lu)\right. \tag{A-8}$$

The index *n* corresponds to the diffraction orders produced by the periodic blazed profile. The height for these diffraction orders is given by the product with the shifted *sinc* calculated in Eq. (A-7). Thus, only the orders contained inside of the width, *2/P*, of the principal maximum of the *sinc* have a significant height.

We see in Eq. (A-8) that the sampling produced by the pixel structure of the LCSLM generates different replicas, labeled with the index *k*, of the diffraction orders of the blazed grating. We can consider that there is no aliasing between the different replicas, separated by a distance *1/D.* This is correct because the separation between replicas, *1/D*, is larger than the distance, *2/P*, where the diffraction orders of the blazed grating have a significant height. This simplifies the analysis because we can study independently each one of the replicas. In principle we are just interested in the replica corresponding to the *0*-order of the pixelation, i.e. *k=0*,

$$T_{k=0}(u)=\left[WDP^2\sum_{n=-\infty}^{+\infty}\delta\left(u-n\frac{1}{P}\right)sinc\left[P\left(u-\frac{f_0}{2pP}\right)\right]sinc(Wu)\right]\otimes L\ sinc(Lu) \tag{A-9}$$

We observe that the height of the diffraction orders *n* produced by the blazed grating is given by the product with the shifted *sinc* already commented and the product with the function *sinc(Wu).* The diffraction orders *n* are then convolved by the function *sinc(Lu)*. This *sinc* function has a width equal to *2/L* for its principal maximum. In principle, this width is very small in comparison with the separation *1/P* between the different orders *n*. Thus, we can approximate the sinc functions by delta functions using the identity

$$\lim_{L\to\infty} L\,sinc(Lu)=\delta(u) \tag{A-10}$$

Thus, Eq. (A-10) can be simplified as

$$T_{k=0}(u) = WDP^2 \sum_{n=-\infty}^{+\infty} \delta\left(u - n\frac{1}{P}\right) sinc\left[P\left(u - \frac{f_0}{2\pi P}\right)\right] sinc(Wu) \qquad \text{(A-11)}$$

Apart from common factors, the expression for the diffraction efficiency $T_n$ (in amplitude) for the *n-th* diffraction order of the blazed grating is given by,

$$T_n = sinc\left(n - \frac{f_0}{2\pi}\right) sinc\left(Wn\frac{1}{P}\right) \qquad \text{(A-12)}$$

The width of a period of the blazed profile can be expressed as $P=pD$, where $p$ is in general a real positive number. We note that the analytical expression given in Eq. (A-4) is general enough to include the case when the period of the blazed grating $P$ is not a multiple number of pixels. With this substitution, $P=pD$, we obtain a more convenient expression for the diffraction efficiencies of the blazed grating,

$$T_n = sinc\left(n - \frac{f_0}{2\pi}\right) sinc\left(n\frac{1}{p}\frac{W}{D}\right) \qquad \text{(A-13)}$$

As we will see, for the purposes of this Appendix we are mainly interested in the diffraction efficiency for the first order, $n=1$, for a blazed grating with a phase depth $f_0 = 2\pi$. As a result, we obtain

$$T_{n=1}(f_0 = 2\pi) = sinc\left(\frac{1}{p}\frac{W}{D}\right) \qquad \text{(A-14)}$$

In Figure A.2 we plot the values given by Eq. (A-14) as a function of the number $p$ of pixels per period. The values of $W$ and $D$ are the ones corresponding to the LCSLM shown in Section 3.5. The ratio $W/D$ is equal to 0.83. We can see that the diffraction efficiency has a fast increase: for $p = 3$ pixels/period the diffraction efficiency is already higher than 0.8. The diffraction efficiency tends to a saturation behavior.

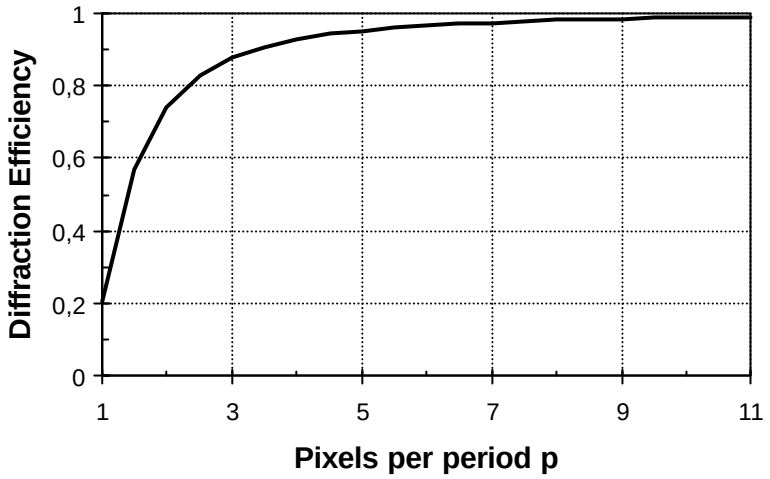


**Figure A.2.** Diffraction efficiency (in amplitude) for the first diffraction order *n=1* as a function of the number of pixels per period *p*. We consider a blazed grating with a phase depth of $2\pi$ radians. The values for *W* and *D* are the ones corresponding to the LCSLM shown in Section 3.5, thus, *W=0.83 D*.

We note in Figure A.2 that for *p = 1* the diffraction efficiency is higher than zero. This result may look incorrect because for *p = 1* no blazed grating profile exists on the LCSLM. Let us analyse this particular case so that we can fully understand Eq. (A-14). For *p=1* the period of the grating is equal to the separation between the pixels, i.e. *P = D*. Thus, the first diffraction order *n=1* in Eq. (A-14) is actually expressing the first diffraction order produced by the pixelation. We can distinguish two different cases. When *W<D* we have a binary amplitude grating on the LCSLM, composed of the dead areas and the clear apertures of the pixels. In this case Eq. (A-14) expresses the light directed into the first diffraction order of this binary amplitude grating. When *W=D* the LCSLM is acting as a monopixel device and no light is diffracted. Thus, in this case the diffraction efficiency for the order *n=1* given by Eq. (A-14) is zero.

Till this point we have discussed the case of the phase-blazed grating displayed on a pixelated device. Now we concentrate our attention on the case of the Fresnel lenses encoded on a pixelated device, such as the LCSLM. For the sake of simplicity we consider the one-dimensional case, i.e. a cylindrical lens. In Figure A.3 we show the phase profile for a one-dimensional lens displayed on a pixelated device.

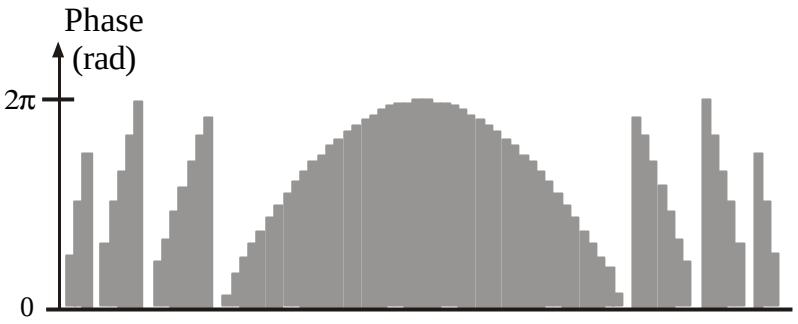


**Figure A.3.** Phase profile for a multilevel diffractive Fresnel lens.

In Figure A.3 we observe the stepped profile due to the pixelation. We also observe that the phase values are restricted to a maximum of $2\pi$ radians.The Fresnel lens can be viewed as a phase blazed grating with a spatially variable period *P* and with a phase depth $\phi_0 = 2\pi$.

In the blazed grating the diffraction orders are located on a plane parallel to the plane of the grating. In the case of the Fresnel lens, the diffraction orders are located along the symmetry axis perpendicular to the lens. We consider a collimated beam of light incident perpendicular to the plane of the Fresnel lens. The zero diffraction order *n=0* for the pixelated Fresnel lens corresponds to the light not deviated by the lens. The first order, *n=1*, corresponds to the light focused at a distance *f* from the plane of the lens, where *f* is the focal length of the lens. We note that as it is a cylindrical lens the focus of the lens is a line. The remaining positive orders *n* correspond to the light focused into secondary foci located at submultiple distances *f/n* along the optical axis. The negative orders *-n* correspond to diverging light as if produced by a diverging lens with focal length *-f/n*.

In this Appendix, as in Section 3.5, we are interested in the light directed into the focus of the lens, i.e. diffraction order *n=1*. The diffraction efficiency for the order *n=1* and for a phase depth $\phi_0 = 2\pi$ is given by Eq. (A-14). In the Fresnel lens, the local number of pixels $p(x)$ per period is not constant. Thus, the diffraction efficiency across the lens is not a constant value. This locally varying diffraction efficiency can be thought as an equivalent amplitude filter multiplying

the Fresnel lens. Using Eq. (A-14), it is trivial to calculate the amplitude profile $t(x)$ across the aperture of the lens for this equivalent filter,

$$t(x) = sinc\left( \frac{1}{p(x)} \frac{W}{D} \right) \tag{A-15}$$

Now, we calculate the local number of pixels $p(x)$ per period due to the quadratic phase profile $j(x)$ of the lens

$$j(x) = \frac{p}{lf} x^2 \tag{A-16}$$

where $l$ and $f$ are respectively the wavelength of the incident light and the focal length of the lens. The phase variation $Dj$ across the length of a period $P=pD$ is given by

$$Dj = j\left( x + {pD}/{2} \right) - j\left( x - {pD}/{2} \right) \tag{A-17}$$

Taking into account that each period presents a phase variation $Dj$ equal to the phase depth $f_0 = 2p$ we can write,

$$\frac{p}{lf}\left[ \left( x + \frac{pD}{2} \right)^2 - \left( x - \frac{pD}{2} \right)^2 \right] = 2p \tag{A-18}$$

After some algebraic manipulations the simplified expression is

$$\frac{p}{lf} 2xpD = 2p \tag{A-19}$$

And the resultant expression for the local number of pixels $p(x)$ is expressed by

$$p(x) = \frac{lf}{xD} \tag{A-20}$$

Finally, we substitute Eq. (A-20) into Eq. (A-15) and we obtain the expression for the equivalent amplitude transmission $t(x)$ across the aperture of the lens

$$t(x) = sinc\left(\frac{Wx}{lf}\right) \tag{A-21}$$

Thus, following a different formalism we have obtained an identical expression to Eq. (3-28) obtained in Section 3.5.1. With the approach developed in this Appendix we have obtained a more intuitive explanation: the non-uniform amplitude profile $t(x)$ can be viewed as originated by the local change in the diffraction efficiency across the aperture of the lens. This change in the diffraction efficiency is produced by the variation in the number of pixels $p(x)$ per period. It is important to note that the profile $t(x)$ is controlled by the clear aperture width *W* instead of the distance between pixels *D.*

We note that in the theoretical development in Section 3.5.1 our goal was to calculate the PSF for a pixelated lens. The resulting PSF was equal to the PSF for a non-pixelated lens convolved by the function describing the shape of the pixel. In this Appendix the strategy has been to calculate the local diffraction efficiency $t(x)$ across the aperture of the lens. The PSF is then obtained by Fourier transforming the function $t(x)$, which is limited by the finite extent *L* of the lens. This leads to the same expression Eq. (3-27) as in Section 3.5.1.

The results presented in this Appendix can be extrapolated to two dimensional lenses displayed on a pixelated device. The quadratic phase $j(x, y)$ for a two dimensional lens is described by

$$j(x, y) = \frac{p}{lf}\left(x^2 + y^2\right) \tag{A-22}$$

This 2D function can be expressed as a product of the separable functions

$$j(x, y) = j(x)j(y) \tag{A-23}$$

where the separable functions are given by Eq. (A-16). Thus, the same arguments applied to $j(x)$ can now be applied to $j(y)$ to obtain the expression for the equivalent amplitude transmission $t(y)$ across the aperture of the lens. Taking

into account that the pixel shape in the LCSLMs that we use is square and with a pixel width $W$ the actual equivalent apodizing function in the two dimensions $(x,y)$ is

$$\tau(x,y) = sinc\left(\frac{Wx}{\lambda f}\right) sinc\left(\frac{Wy}{\lambda f}\right) \qquad \text{(A-24)}$$

which is equal to the expression in Eq. (3-29) in Section 3.5.1. This approach is valid for rectangular pixels. In the general case when the pixel shape is not rectangular we would use the formalism followed in Section 3.5.1.

Finally, we mention that the general expression that we have obtained for the diffraction efficiency, Eq. (A-13), can be used as the starting point to analyse other DOEs displayed on a pixelated device with more general phase profiles $\varphi(x)$.

# REFERENCES

[PAPER A] A. Márquez, J. Campos, M. J. Yzuel, I. Moreno, J. A. Davis, C. Iemmi, A. Moreno and A. Robert, "Characterization of edge effects in twisted nematic liquid crystal displays", Opt. Eng. 39, 3301-3307 (2000).

[PAPER B] A. Márquez, C. Iemmi, I. Moreno, J. A. Davis, J. Campos and M. J. Yzuel, "Quantitative prediction of the modulation behavior of twisted nematic liquid crystal displays based on a simple physical model", accepted for publication in Optical Engineering.

[PAPER C] J. A. Davis, J. C. Escalera, J. Campos, A. Márquez, M. J. Yzuel and C. Iemmi, "Programmable axial apodizing and hyperresolving amplitude filters using a liquid crystal spatial light modulator", Opt. Lett. 24, 628-630 (1999).

[PAPER D] M. J. Yzuel, J. Campos, A. Márquez, J. C. Escalera, J. A. Davis, C. Iemmi and S. Ledesma, "Inherent apodization of lenses encoded on liquid crystal spatial light modulators", Appl. Opt. 39, 6034-6039 (2000).

[PAPER E] A. Márquez, C. Iemmi, J. C. Escalera, J. Campos, S. Ledesma, J. A. Davis and M. J. Yzuel, "Amplitude apodizers encoded onto Fresnel lenses implemented on a phase-only spatial light modulator", Appl. Opt. 40, 2316-2322 (2001).

[Air35] G. B. Airy, "On the diffraction of an object-glass with circular aperture", Trans. Camb. Phil. Soc. 5, 283-291 (1835).

[Ama90] J. Amako and T. Sonehara, "Computer-generated hologram using TFT active matrix liquid crystal spatial light modulator (TFT-LCSLM)", Jpn. J. Appl. Phys. 29, L1533-L1535 (1990).

[Arr99] V. Arrizón, E. Carreón and L. A. González, "Self apodization of low-resolution pixelated lenses", Appl. Opt. 38, 5073-5077 (1999).

[Aur72] L. d'Auria, J. P. Huignard, A. M. Roy and E. Spitz, "Photolithographic fabrication of thin film lenses", Opt. Commun. 5, 232-235 (1972).

[Azz72] R. M. A. Azzam and N. M. Bashara, “Simplified approach to the propagation of polarized light in anisotropic media-Application to liquid crystals”, J. Opt. Soc. Am. 62, 1252-1257 (1972).

[Bar89] T. H. Barnes, T. Eiju, K. Matsuda and N. Ooyama, “Phase-only modulation using a twisted nematic liquid crystal television”, Appl. Opt. 28, 4845-4852 (1989).

[Ber95] A. Bergeron, J. Gauvin, F. Gagnon, D. Gingras, H. H. Arsenault and M. Doucet, “Phase calibration and applications of a liquid-crystal spatial light modulator”, Appl. Opt. 34, 5133-5139 (1995).

[Ber72] D. W. Berreman, “Optics in stratified and anisotropic media: 4x4-matrix formulation”, J. Opt. Soc. Am. 62, 502-510 (1972).

[Ber73] D. W. Berreman, “Optics in smoothly varying anisotropic planar structures: Application to liquid-crystal twist cells”, J. Opt. Soc. Am. 63, 1374-1380 (1973).

[Ber74] D. W. Berreman, “Dynamics of liquid-crystal twist cells”, Appl. Phys. Lett. 25, 12-15 (1974).

[Ber75] D. W. Berreman, “Liquid-crystal twist cell dynamics with backflow”, J. Appl. Phys. 46, 3746-3751 (1975).

[Bol98] G. T. Bold, T. H. Barnes, J. Gourlay, R. M. Sharples and T. G. Haskell, “Practical issues for the use of liquid crystal spatial light modulators in adaptive optics”, Opt. Commun. 148, 323-330 (1998).

[Bor88] G. D. Boreman and E. R. Raudenbush, “Modulation depth characteristics of a liquid crystal television spatial light modulator”, Appl. Opt. 27, 2940-2943 (1988).

[Bou97] J. L. de Bougrenet de la Tocnaye and L. Dupont, “Complex amplitude modulation by use of liquid-crystal spatial light modulators,” Appl. Opt. 36, 1730-1741 (1997).

[Bro95] R. J. Broessel, V. Dominic and R. C. Hardie, “Image restoration of dispersion-degraded images from a liquid-crystal beam steerer”, Opt. Eng. 34, 3138-3145 (1995).

[Cam89] J. Campos and M.J. Yzuel, “Axial and extra-axial response in aberrated optical systems with apodizers. Optimization of the Strehl ratio”, J. Mod. Opt. 36, 733-749 (1989).

[Cam00a] J. Campos, J.C. Escalera, C.J.R. Sheppard and M.J. Yzuel, “Axially invariant pupil filters”, J. Mod. Opt. 47, 57-68 (2000).

[Cam00b] J. Campos, A. Márquez, M. J. Yzuel, J. A. Davis, D. M. Cottrell and I. Moreno, “Fully complex synthetic discriminant functions written onto phase-only modulators”, Appl. Opt. 39, 5965-5970 (2000).

[Car94a] E. Carcolé, J. Campos and S. Bosch, “Diffraction theory of Fresnel lenses encoded in low-resolution devices”, Appl. Opt. 33, 162-174 (1994).

[Car94b] E. Carcolé, J. Campos, I. Juvells and S. Bosch, “Diffraction efficiency of low-resolution Fresnel encoded lenses”, Appl. Opt. 33, 6741-6746 (1994).

[Car95] E. Carcolé, J. Campos, I. Juvells and J. R. de F. Moneo, “Diffraction theory of optimized low-resolution Fresnel encoded lenses”, Appl. Opt. 34, 5952-5960 (1995).

[Che97] C.-J. Chen, A. Lien and M. I. Nathan, "Simple method for the calculation of the deformation profiles in chiral nematic liquid crystal cells with asymmetric pretilt", J. Appl. Phys. 81, 70-73 (1997).

[Chi99] V. G. Chigrinov, Liquid crystal devices: physics and applications, Artech House (1999).

[Chu88] C.S Chung and H.H. Hopkins, "Influence of non-uniform amplitude on PSF", J. Mod. Opt. 35, 1485-1511 (1988).

[Cot90] D. M. Cottrell, J. A. Davis, T. R. Hedman and R. A. Lilly, "Multiple imaging phase-encoded optical elements written as programmable spatial light modulators", Appl. Opt. 29, 2505-2509 (1990).

[Coy96] J. A. Coy, M. Zaldarriaga, D. F. Grosz and O. E. Martínez, "Characterization of a liquid crystal television as a programmable spatial light modulator", Opt. Eng. 35, 15-19 (1996).

[Dal80] W. J. Dallas, "Computer generated holograms", in B. R. Frieden, editor, The computer in optical research, chapter 6, 291-366, Springer-Verlag, Berlin (1980).

[Dav89a] J. A. Davis, D. M. Cottrell, R. A. Lilly and S. W. Connely, "Multiplexed phase encoded lenses written on spatial light modulators", Opt. Lett. 14 , 420-422 (1989).

[Dav89b] J. A. Davis, D. M. Cottrell, J. E. Davis and R. A. Lilly, "Fresnel lens-encoded binary phase-only filters for optical pattern recognition", Opt. Lett. 14 , 659-661 (1989).

[Dav92] J. A. Davis, H. M. Schley-Seebold and D. M. Cottrell, "Anamorphic optical systems using programmable spatial light modulators", Appl. Opt. 31, 6185-6186 (1992).

[Dav98] J. A. Davis, I. Moreno and P. Tsai, "Polarization eigenstates for twisted-nematic liquid crystal displays," Appl. Opt. 37, 937-945 (1998).

[Dav99a] J. A. Davis, D. B. Allison, K. G. D'Nelly, M. L. Wilson and I. Moreno, "Ambiguities in measuring the physical parameters for twisted-nematic liquid crystal spatial light modulators," Opt. Eng. 38, 705-709 (1999).

[Dav99b] J. A. Davis, P. Tsai, K. G. D'Nelly and I. Moreno, "Simple technique for determining the extraordinary axis direction for twisted-nematic liquid crystal spatial light modulators", Opt. Eng. 38, 929-932 (1999).

[Dav99c] J. A. Davis, P. Tsai, D. M. Cottrell, T. Sonehara and J. Amako, "Transmission variations in liquid crystal spatial light modulators caused by interference and diffraction effects", Opt. Eng. 38, 1051-1057 (1999).

[Dav99d] J.A. Davis, D.M. Cottrell, J. Campos, M.J. Yzuel and I. Moreno, "Encoding amplitude information onto phase only filters", Appl. Opt. 38, 5004-5013 (1999).

[Doo75] C. Z. van Doorn, "Dynamic behavior of twisted nematic liquid-crystal layers in switched fields", J. Appl. Phys. 46, 3738-3745 (1975).

[Dou95] R. Dou and M. K. Giles, "Closed-loop adaptive optics system with a liquid crystal television as a phase retarder", Opt. Lett. 20, 1583-1585 (1995).

[Efr95] U. Efron, editor, Spatial light modulator technology: materials, devices and applications, Marcel Dekker, New York (1995).

[Eri61] J. L. Ericksen, Trans. Soc. Rheol. 5, 23 (1961).

[Esc94] J. C. Escalera, J. Campos and M. J. Yzuel, "Pupil symmetries for identical axial response", Microwave Opt. Technol. Lett. 7, 174-178 (1994).

[Fer00] C. R. Fernández-Pousa, I. Moreno, N. Bennis and C. Gómez-Reino, "Generalized formulation and symmetry properties of reciprocal nonabsorbing polarization devices: application to liquid-crystal displays", J. Opt. Soc. Am. A 17, 2074-2080 (2000).

[Fer94] M. Ferstl, B. Kuhlow and E. Pawlowski, "Effect of fabrication errors on multilevel Fresnel zone lenses", Opt. Eng. 33, 1229-1235 (1994).

[Fer96] M. Ferstl and A. M. Frisch, "Static and dynamic Fresnel zone lenses for optical interconnections", J. Mod. Opt. 43, 1451-1462 (1996).

[Fim94] A. Fimia, R. Fuentes, I. Pascual, A. Beléndez, J. J. Egozcue and M. T. Navarro, "Copying computer-generated-holographic interconnects by the use of partially coherent light", Appl. Opt. 33, 1431-1433 (1994).

[Fra58] F. C. Frank, "On the theory of liquid crystals", Discuss. Faraday Soc. 25, 19-28 (1958).

[Fuk93] H. Fukuda, Y. Kobayashi, K. Hama, T. Tawa and S. Okazaki, "Evaluation of pupil-filtering in high-numerical aperture I-line lens", Jpn. J. Appl. Phys. 32, 5845-5849 (1993).

[Gen93] P. G. de Gennes and J. Prost, The physics of liquid crystals, chapter 3, p. 98-150, Oxford Science Publications, 2nd edition, (1993).

[Gon95] L. Gonçalves Neto, D. Roberge and Y. Sheng, "Programmable optical phase-mostly holograms with coupled-mode modulation liquid crystal television", Appl. Opt. 34, 1944-1950 (1995).

[Gon96] L. Gonçalves Neto, D. Roberge and Y. Sheng, "Full-range, continuous, complex modulation by the use of two coupled-mode liquid-crystal televisions", Appl. Opt. 35, 4567-4576 (1996).

[Goo75] C. H. Gooch and J. A. Tarry, "The optical properties of twisted nematic liquid crystal structures with twist angles ≤ 90º", J. Phys. D.: Appl. Phys. 8, 1575-1584 (1975).

[Goo96] J. W. Goodman, Introduction to Fourier Optics, McGraw-Hill, 2nd edition, (1996).

[Gre86] D. A. Gregory, "Real-time pattern recognition using a modified liquid crystal television in a coherent optical correlator", Appl. Opt. 25, 467-469 (1986).

[Gre92] D. A. Gregory, J. C. Kirsch and E. C. Tam, "Full complex modulation using liquid-crystal televisions", Appl. Opt. 31, 163-165 (1992).

[Gri76] J. Grinberg and A. D. Jacobson, "Transmission characteristics of a twisted nematic liquid-crystal layer", J. Opt. Soc. Am. 66, 1003-1009 (1976).

[Hai01] M. Hain, R. Glöckner, S. Bhattacharya, D. Dias, S. Stankovic and T. Tschudi, "Fast switching liquid crystal lenses for a dual focus digital versatile disc pickup", Opt. Commun. 188, 291-299 (2001).

[Hee75] E. W. S. Hee, "Fabrication of apodized apertures for laser beam attenuation", Opt. Laser Tech. 4, 75-79 (1975).

[Heg86] Z. S. Hegedus and V. Sarafis, "Superresolving filters in confocally scanned imaging systems", J. Opt. Soc. Am. A 3, 1892-1896 (1986).

[Her96] H. P. Herzig, editor, Micro-optics, Taylor & Francis, London (1996).

[Hil95] R. Hild, J.C. Escalera, M.J. Yzuel; and R. Muschall, "Point spread function and coherent line response in optical systems with non-uniform transmission pupils: application to photolithography", Pure Appl. Opt., 14, 795-810 (1995)

[Hop49] H. H. Hopkins, Proc. Phys. Soc. B 62, 22 (1949).

[Hop50] H. H. Hopkins, Wave aberration theory, Oxford Clarendon Press (1950).

[Hop70] H. H. Hopkins and M. J. Yzuel, "The computation of diffraction patterns in the presence of aberrations", Optica Acta 17, 157-182 (1970).

[Hua93] S. Huard, Polarisation de la lumière, Masson, Paris (1993).

[Jac92] S. D. Jacobs, editor, Selected papers on liquid crystals for optics, SPIE Milestone Series Vol. MS 46 (1992).

[Jac64] P. Jacquinot and B. Roizen-Dossier, "Apodisation", in E. Wolf Ed., Progress in Optics, Vol. 3, North-Holland, (1964).

[Jav86] B. Javidi, and F.T.S. Yu, "Real-time image recognition by partially coherent light", Appl. Opt. 25, 2365-2371 (1986).

[Jav94] B. Javidi, J. Horner, Ed. Real-time opticl information processing, Academic Press, San Diego (1994).

[Jud93] R. D. Juday, "Optimal realizable filters and the minimum Euclidean distance principle", Appl. Opt. 32, 5100-5111 (1993).

[Kel98] T.-L. Kelly and J. Munch, "Wavelength dependence of twisted nematic liquid crystal phase modulators", Opt. Commun. 156, 252-258 (1998).

[Kel01] S. M. Kelly and M. O'Neill, "Liquid crystals for electro-optic applications", in H. S. Nalwa Ed., Handbook of advanced electronic and photonic materials and devices, Volume 7, chapter 1, Academic Press, (1995).

[Kir71] J. P. Kirk and A. L. Jones, "Phase-only complex-valued spatial filter", J. Opt. Soc. Am. 61, 1023-1028 (1971).

[Kir92] J. C. Kirsch, D. A. Gregory, M. W. Thie and B. K. Jones, "Modulation characteristics of the Epson liquid crystal television", Opt. Eng. 31, 963-970 (1992).

[Kon88] N. Konforti, E. Marom and S.-T. Wu, "Phase-only modulation with twisted nematic liquid-crystal spatial light modulators", Opt. Lett. 13, 251-253 (1988).

[Kud97] A. V. Kudryashov, J. Gonglewski, S. Browne and R. Highland, "Liquid crystal phase modulator for adaptive optics. Temporal performance characterization", Opt. Commun. 141, 247-253 (1997).

[Lab00] I. Labastida, A. Carnicer, E. Martín-Badosa, S. Vallmitjana and I. Juvells, "Optical correlation by use of partial phase-only modulation with VGA liquid-crystal displays", Appl. Opt. 39, 766-769 (2000).

[Lau94] V. Laude and Ph. Réfrégier, "Multicriteria characterization of coding domains with optimal Fourier spatial light modulators filters", Appl. Opt. 33, 4465-4471 (1994).

[Lau98] V. Laude, "Twisted-nematic liquid-crystal pixelated active lens", Opt. Commun. 153, 134-152 (1998).

[Led98] S. Ledesma, C. Iemmi, J. Campos and M. J. Yzuel, "Joint transform correlator architecture with a single LCTV operating in phase-mostly mode", Opt. Commun. 151, 101-109 (1998).

[Les68] F. M. Leslie, Arch. Rat. Mech. Anal. 28, 265 (1968).

[Lie90] A. Lien, "Extended Jones matrix representation for the twisted nematic liquid-crystal display at oblique incidence", Appl. Phys. Lett. 57, 2767-2769 (1990).

[Liu85] H.-K. Liu, J. A. Davis and R. A. Lilly, "Optical-data-processing properties of a liquid-crystal television spatial light modulator," Opt. Lett. 10, 635-637 (1985).

[Liu89] H.-K. Liu and T.-H. Chao, "Liquid crystal television spatial light modulators," Appl. Opt. 28, 4772-4780 (1989).

[Loh67] A. W. Lohman and D. P. Paris, "Binary Fraunhofer holograms, generated by computer", Appl. Opt. 6, 1739-1748 (1967).

[Lop98] O. López-Coronado, I. Moreno, J. Campos and M. J. Yzuel, "Full in situ characterization of spatial light modulators in an optical correlator. Filter adaptation to operating curves", J. Mod. Opt. 45, 2461-2472 (1998).

[Lov94] G. D. Love, J. V. Major and A. Purvis, "Liquid-crystal prisms for tip-tilt adaptive optics", Opt. Lett. 19, 1170-1172 (1994).

[Lov97] G. D. Love, "Wave-front correction and production of Zernike modes with a liquid-crystal spatial light modulator", Appl. Opt. 36, 1517-1524 (1997).

[Lu90] K. Lu and B. E. A. Saleh, "Theory and design of the liquid crystal TV as an optical spatial phase modulator", Opt. Eng. 29, 240-246 (1990).

[Lu91a] K. Lu and B. E. A. Saleh, "Complex amplitude reflectance of the liquid crystal light valve", Appl. Opt. 30, 2354-2362 (1991).

[Lu91b] K. Lu and B. E. A. Saleh, "Optimal twist and polarizations angles for the reflective liquid crystal modulator", J. Mod. Opt. 38, 2401-2411 (1991).

[Mar00] A. Márquez, J. Campos, M. J. Yzuel, I. Pascual, A. Fimia and A. Beléndez, "Production of computer-generated phase holograms using graphic devices. application to correlation filters", Opt. Eng. 39, 1612-1619 (2000).

[Mar01] A. Márquez, M. Yamauchi, J. A. Davis and D. J. Franich, "Phase measurements of a twisted nematic liquid crystal spatial light modulator with a common-path interferometer", Opt. Commun. 190, 129-133 (2001).

[McM93] P. F. McManamon, E. A. Watson, T. A. Dorschner and L. J. Barnes, "Applications look at the use of liquid crystal writable gratings for steering passive radiation", Opt. Eng. 32, 2657-2664 (1993).

[Mil86] J.P. Mills and B.J. Thompson, "Effect of aberrations and apodization on the performance of coherent optical systems. I. The amplitude impulse response", J. Opt. Soc. Am. 3, 694-703 (1986).

[Mil96] J. P. Mills and B. J. Thompson, editors, Selected papers on apodization-coherent optical systems, SPIE Milestone Series Vol. MS 119 (1996).

[Mor95a] I. Moreno, C. Gorecki, J. Campos, M. J. Yzuel, “Comparison of computer-generated holograms produced by laser printers and litography: application to pattern recognition”, Opt. Eng. 34, 3520-3525 (1995).

[Mor95b] I. Moreno, J. Campos, C. Gorecki and M. J. Yzuel, “Effects of amplitude and phase mismatching errors in the generation of a kinoform for pattern recognition“, Jap. J. Appl. Phys. 34, 6423-6434 (1995).

[Mor98a] I. Moreno, J. A. Davis, K. G. D'Nelly and D. B. Allison, “Transmission and phase measurement for polarization eigenvectors in twisted-nematic liquid crystal spatial light modulators”, Opt. Eng. 37, 3048-3052 (1998).

[Mor98b] I. Moreno, N. Bennis, J. A. Davis and C. Ferreira, “Determination of the twist angle in twisted nematic liquid crystal by location of local adiabatic points”, Opt. Commun. 158, 231-238 (1998).

[Nis87] H. Nishihara and T. Suhara, “Micro Fresnel lenses”, in E. Wolf Ed., Progress in Optics, Vol. 24, Elsevier Science Publishers, Amsterdam, (1964).

[Ohk93] K. Ohkubo and J. Ohtsubo, “Evaluation of LCTV as a spatial light modulator”, Opt. Commun. 102, 116-124 (1993).

[Oje86] J. Ojeda-Castañeda, P. Andrés and A. Díaz, “Annular apodizers for low sensitivity to defocus and to spherical aberration”, Opt. Lett. 11, 487-489 (1986).

[Ong88] H. L. Ong, “Origin and characteristics of the optical properties of general twisted nematic liquid crystal displays”, J. Appl. Phys. 64, 614-628 (1988).

[Ose33] C. W. Oseen, Trans. Faraday Soc.29, 883 (1933).

[Oto90] J. M. Otón, J. M. Sánchez, J. L. Pinter and A. Serrano, “Cristales líquidos: una panorámica (I)”, Mundo Electrónico 207, 99-105 (1990).

[Pas92] I. Pascual, A. Beléndez and A. Fimia, “Holographic system for copying holograms by using partially coherent light”, Appl. Opt. 31, 3312-3319 (1992).

[Pas00] I. Pascual, A. Márquez, A. Beléndez, A. Fimia, J. Campos and M. J. Yzuel, “Copying low spatial frequency diffraction gratings in photopolymer as phase holograms”, J. Mod. Opt. 47, 1089-1097 (2000).

[Pez93] J. L. Pezzanitti and R. A. Chipman, “Phase-only modulation of a twisted nematic liquid-crystal TV by use of the eigenpolarization states”, Opt. Lett. 18, 1567-1569 (1993).

[Sch71] M. Schadt and W. Helfrich, “Voltage-dependent optical activity of a twisted nematic liquid crystal”, Appl. Phys. Lett. 18, 127-128 (1971).

[Sch97] M. Schmitz and O. Bryngdahl, “Rigorous concept for the design of diffractive microlenses with high numerical apertures”, J. Opt. Soc. Am. A 14, 901-906 (1997).

[Ser99] S. Serati and K. Bauchert, “SLMs meet the challenge of new applications”, Laser Focus World, May 1999, 229-233.

[She88] C. J. R. Sheppard and Z. S. Hegedus, “Axial behavior of pupil plane filters”, J. Opt. Soc. Am. A, 5, 643-647 (1988).

[Sou94a] C. Soutar, S. E. Monroe, Jr. and J. Knopp, “Measurement of the transmittance of the Epson liquid crystal television”, Opt. Eng. 33, 1061-1068 (1994).

[Sou94b] C. Soutar and K. Lu, “Determination of the physical properties of an arbitrary twisted-nematic liquid crystal cell”, Opt. Eng. 33, 2704-2712 (1994).

[Sto91] T. W. Stone and B. J. Thompson, editors, Selected papers on holographic and diffractive lenses and mirrors, SPIE Milestone Series Vol. MS 34 (1991).

[Str35] R. Straubel, Pieter Zeeman Verhandelingen, Martinus Nijhoff, 302 (1935).

[Str94] K. Strehl, Die Beugungstheorie des Femrohrs, Leipzig, Barth (1894).

[Str79] J. W. Strut (Lord Rayleigh), Philos. Mag. 8, 403 (1879).

[Tab90] D. B. Taber, J. A. Davis, L. A. Holloway, Jr. and O. Almagor, "Optically controlled Fabry-Perot interferometer using a liquid crystal light valve", Appl. Opt. 29, 2623-2631 (1990).

[Tak96] Y. Takaki and H. Ohzu, "Reconfigurable lens with an electro-optical learning system", Appl. Opt. 35, 6896-6908 (1996).

[Tam92a] E. C. Tam, S. Zhou and M. R. Feldman, "Spatial-light-modulator-based electro-optical imaging system", Appl. Opt. 31, 578-580 (1992).

[Tam92b] E. C. Tam, "Smart electro-optical zoom lens", Opt. Lett. 17, 369-371 (1992).

[Thu81] R. N. Thurston and D. W. Berreman, "Equilibrium and stability of liquid-crystal configurations in an electric field", J. Appl. Phys. 52, 508-509 (1981).

[Tor52] G. Toraldo di Francia, "Super-gain antennas and optical resolving power", Nuovo Cimento 9, 426-438 (1952).

[Tur97] J. Turunen and F. Wyrowski, Diffractive optics for industrial and commercial applications, Akademie Verlag, Berlin (1997).

[Wan00] X. Wang, D. Wilson, R. Muller, P. Maker and D. Psaltis, "Liquid-crystal blazed-grating beam deflector", Appl. Opt. 39, 6545-6555 (2000).

[Wu95] S.-T. Wu, "Nematic liquid crystals", in U. Efron Ed., Spatial light modulator technology: materials, devices and applications, chapter 1, 1-31, Marcel Dekker, New York (1995).

[Yam95a] M. Yamauchi and T. Eiju, "Optimization of twisted nematic liquid crystal panels for spatial light phase modulation", Opt. Commun. 115, 19-25 (1995).

[Yam95b] M. Yamauchi and T. Eiju, "Phase modulation capability of thin twisted nematic liquid crystal panels at double-pass configurations", Opt. Rev. 2, 24-27 (1995).

[Yam00] M. Yamauchi, A. Márquez, J. D. Davis and D. J. Franich, "Interferometric phase measurements for polarization eigenvectors in twisted nematic liquid crystal spatial light modulators", Opt. Commun. 181, 1-6 (2000).

[Yan00] D.-K. Yang and X.-D. Mi, "Modelling of the reflection of cholesteric liquid crystals using the Jones matrix", J. Phys. D: Appl. Phys. 33, 672-676 (2000).

[Yar84] A. Yariv and P. Yeh, Optical waves in crystals, chapter 5, 121-154, John Wiley & Sons (1984).

[Yeh99] P. Yeh and C. Gu, Optics of liquid crystal displays, John Wiley & Sons (1999).

[Yzu79] M. J. Yzuel and F. Calvo, "A study of the possibility of image optimization by apodization filters in optical systems with residual aberrations", Optica Acta 26, 1397-1406 (1979).

[Yzu80] M. J. Yzuel and F. J. Arlegui, "A study on the computation accuracy of the aberrational diffraction images", Optica Acta 27, 549-562 (1980).

[Yzu83] M. J. Yzuel and F. Calvo, “Point-spread function calculation for optical systems with residual aberrations and a non-uniform transmission pupil”, Optica Acta 30, 233-242 (1983).

[Yzu88] M. J. Yzuel, J. C. Escalera, G. Cansado and J. Campos, “Illuminance and chromaticity of the image of optical systems with non-uniform transmission filters”, Proc. SPIE 1013, 120-127 (1988).

[Yzu90] M.J. Yzuel, J.C. Escalera and J. Campos, “Polychromatic axial behavior of axial apodizing and hyperresolving filters”, Appl. Opt. 29, 1631-1641 (1990).

[Zha94] Z. Zhang, G. Lu and F. T. S. Yu, “Simple method for measuring phase modulation in liquid crystal televisions”, Opt. Eng. 33, 3018-3022 (1994).

[Zhi98] Y. Zhisheng, L. Yulin, L. Jifang and H. Zhengquan, “Measurement of the phase modulation of liquid-crystal televisions by a noninterferometric technique,” Appl. Opt. 37, 3069-3075 (1998).

**Web links:**

[Hep@] Heptagon Oy is a company dealing with diffractive and refractive micro-optics: http://www.heptagon.fi/

[LCH@] Website for the Liquid Crystal Group in Hamburg with a lot of resources oriented to liquid crystal related research: http://liqcryst.chemie.uni-hamburg.de

[Plc@] Polymers and liquid crystals produced by Case Western Reserve University and Kent State University: http://plc.cwru.edu/

[RPC@] Rochester Photonics Corporation is a company dealing with diffractive and refractive micro-optics: http://www.corning.com/RochesterPhotonics

# List of acronyms

| Acronym | Meaning |
|---|---|
| AOSLM | Acousto-optic spatial light modulator |
| BIP | Best image plane |
| CCD | Charge coupled device |
| CGH | Computer-generated holograms |
| CRT | Cathode ray tube |
| DMD | Deformable mirror devices |
| DOE | Diffractive optical element |
| DOF | Depth of focus |
| DP | Dichroic polymer |
| DVD | Digital versatile disc |
| ECB | Electrically controlled birefringence |
| EOSLM | Electro-optic spatial light modulator |
| FPC | Flexible printed circuit |
| FPD | Flat panel display |
| GGOA | Generalised geometrical-optics approximation |
| GSL | Gray-scale level |
| HOE | Holographic optical element |
| LC | Liquid crystal |
| LCD | Liquid crystal display |
| LCSLM | Liquid crystal spatial light modulator |
| MOSLM | Magneto-optic spatial light modulator |
| MQW | Multiple quantum well |

| Acronym | Meaning |
|---|---|
| PCB | Printed circuit board |
| PSF | Point-spread function |
| SLM | Spatial light modulator |
| STN | Supertwisted nematic |
| TFT | Thin-film transistor |
| TN | Twisted-nematic |
| TV | Television |
| VGA | Video graphics array |